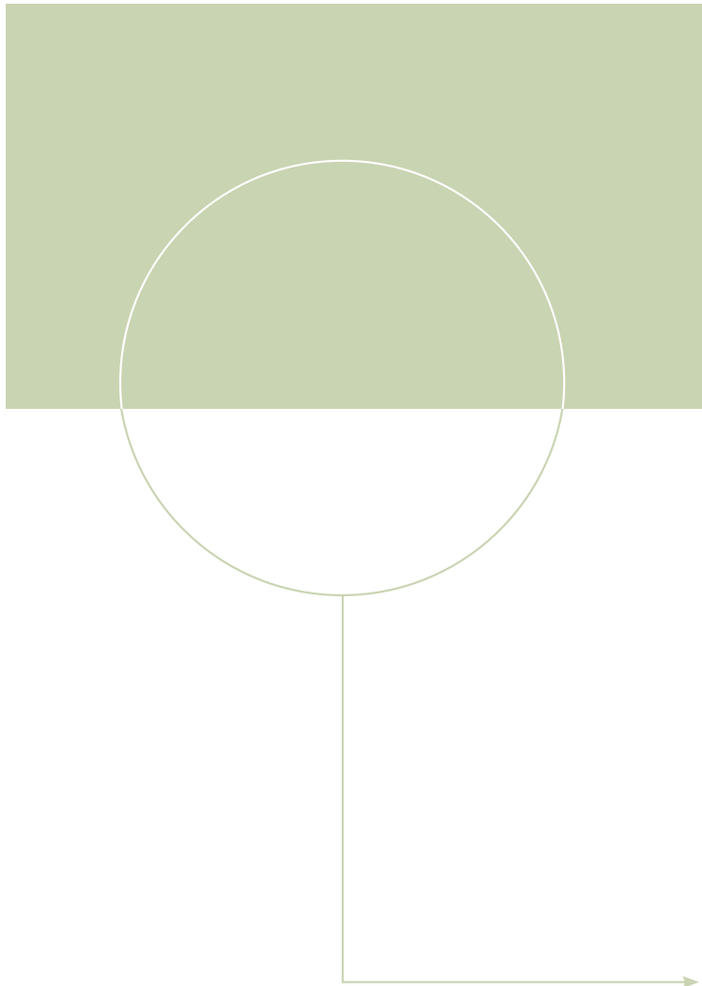

Master's thesis

2019

Muhammad Iffan Hannanu

NTNU
Norwegian University of
Science and Technology
Faculty of Engineering
Department of Geoscience and Petroleum

Muhammad Iffan Hannanu

Lattice Boltzmann Modeling of microfluidic two-phase flow with complex pore structure

June 2019

NTNU
Norwegian University of
Science and Technology

NTNU
Norwegian University of
Science and Technology

NTNU

Norwegian University of
Science and Technology

Lattice Boltzmann Modeling of microfluidic two-phase flow with complex pore structure

Muhammad Iffan Hannanu

Petroleum Engineering
Submission date: June 2019
Supervisor: Carl Fredrik Berg
Co-supervisor: Thomas Ramstad

Norwegian University of Science and Technology
Department of Geoscience and Petroleum

"And He found you lost and guided [you]". Ad-Duhaa [93:7]

Summary

In the past, the technology to capture a high-resolution image was not mature enough to enable pore-scale modeling and simulation. Additionally, including sufficient pore geometry complexities leads to a heavy computational cost. However, as high-resolution image of a pore structure and high performance computing become more availble nowadays, pore-scale simulation is emerging as a powerful tool to predict the flow properties in a porous media.

One of the most common fluid flow simulation method at the pore-scale is Lattice Boltzmann Modeling (LBM). In this method, the fluid is represented with its particle distribution. The fluid particle distribution undergoes two main processes: streaming and collision. streaming part depicts the movement of the particle distribution between lattices. Collision part depicts the relaxation of the particle distribution towards local equilibrium due to particle collision. The LBM method has many advantages: 1) it can be used directly in a digital pore structure, 2) the implementation is simple and straightforward, and 3) well-suited for parallel computing. For the thesis, we are using the open source software LBPM. The software uses $D3Q19$ lattice system and boundary condiitons as described by McClure et al. (2018). The method is extended with colour gradient method to model immiscible two-phase flow.

The focus of the thesis is to observe the first-order effect of LBM parameters to the fluid distribution and flow properties, and how they are correlated with experimental studies. Drainage and imbibition process in a microfluidic experiment are simulated. We are particularly interested in observing the typical displacement mechanism that occur in the simulation, with regards to its viscous and capillary forces.

Preface

Before my arrival in Trondheim, I had few expectations about what I wanted to achieve during my master study. I certainly hoped to learn more about reservoir engineering in general, but I had no definite idea of what to expect. Fortunately, what I have gained in NTNU IGP was much more than what I had expected. Here, I was introduced to many interesting topics that I have never heard of before. Out of all these topics, one topic drew my attention: pore-scale studies. I never would have imagined that I will write a thesis about pore-scale simulation. Previously, I always thought that this topic is mundane and unworthy to get into. However, after I read several literature on the subject, looked at the ongoing research, and consulted with several people, I started to find them appealing. It turned out that I really enjoyed working on the topic.

In the course of two years, I had fun with pore-scale studies. First of all, it all started when my supervisor introduced me to this topic in spring 2018. At that time, I could choose from four different topics, where two of them were pore-scale studies: lattice-Boltzmann modeling (LBM) or pore network modeling. I chose LBM because it appeared more appealing to me. Thereafter, I tried to go through the basics and developed a code for lattice-gas cellular automata (LGCA) with Markus. Then, in summer 2018, I had the opportunity to work on the micromodel experiment in NTNU IGP reservoir lab. Here, not only that I experienced first hand how to set up the experiment and how to observe the fluid flow in the micromodel, I also knew how to obtain pore-structure from digital rock images. In autumn 2018, for my specialization course and specialization project, I focused on the fundamentals of Boltzmann Equation and LBM, then developed an LBM code for single-phase, D2Q9 system. Then, together with Carl, Markus, and Hossein, we developed this code further to model Klinkenberg effect on a pore structure. In spring 2018, I started writing this thesis on LBM simulation on realistic pore structure for two-phase flow. In this thesis, I use LBPM, an open-source code for LBM simulation. The reason was that this code has been developed for years, and includes all the necessary features to run the necessary model.

My personal objective for my master thesis is not only to get a good simulation result, but also to deliver a self-contained document. While writing this document, I found that there is only a handful of literature that gives an extensive and detailed explanation about LBM. Additionally, some literature assume the reader to have a background in some advanced topics. This is one of the biggest challenge that I encountered when dealing with LBM. In this document, however, I attempted to simplify the problem without excluding the essence. Moreover, some parts were already explained in the specialization project document. In that case, the part will be explained briefly, or will be put in the appendix (it is also recommended to read the specialization project document). I really hope that this document can be the future extensive reference for someone who wants to go through LBM for the first time.

Finally, this thesis would not be finished without contribution from many important people in my life. First and foremost, I would like to express my highest regard towards my parents for their affection, love, sacrifices, and supports throughout my life. Then, I would like to say my sincere gratitude to my supervisor, Carl Fredrik Berg, for his thesis advice during the course of the semester. I would also like to appreciate the people who have helped me directly with the thesis: Ole Torsæter, Mohammad Hossein Golestan, Dicky Harishidayat, Markus Hays Nielsen, and Thomas Ramstad. Last but not least, I wanted to say my appreciation to all the members of PPIT (Indonesia Student Association in Trondheim) and KMIT (Indonesian Muslim Family in Trondheim) for their company and help throughout my stay in Trondheim.

I will always cherish what I have gained here in NTNU. These two years have been time well spent.

Muhammad Iffan Hannanu

Table of Contents

List of Tables

List of Figures

Chapter 1

Introduction

Lattice-Boltzmann Modeling (LBM) is emerging as one of the most powerful tools to simulate fluid flow, and has been growing exponentially since 1992 (Sukop and Thorne Jr., 2006). There are many reasons why LBM is popular nowadays. Firstly, in a pore-scale study perspective, LBM is an excellent tool since it fundamentally observe the physics at microscopic scale, while also able to produce the physics at a macroscopic scale. As a consequence, LBM allows many tuning parameters that can be adjusted to satisfy our needs. For instance, LBM allows the modeling of the interaction between fluid-fluid and fluid-solid at microscopic scale, which is essential for a pore-scale study. This comes at the cost of an upscaling problem later on.

Secondly, the implementation of LBM is simple, despite its complex theoretical background. LBM is derived from lattice gas cellular automata (LGCA), where the particle is represented using boolean variables. In LGCA, the particle undergoes two processes: streaming and collision. Streaming process is when the particle moves between two adjacent lattices, while the collision process is when the particles collide and then redistribute in a lattice. These processes are such that the mass and momentum of particles are conserved. A particle n_a that resides at $\vec{x}$ with a velocity c_a at time t will move to a position of $\vec{x} + c_a$ at time $t + 1$. The LGCA equation takes the following form:

$$\left|n_a(\vec{x} + c_a, t + 1)\right\rangle = \left|n_a(\vec{x}, t)\right\rangle + \left|C(n_a)\right\rangle \tag{1.1}$$

where a are the lattice directions, and C is the collision operator. These processes are simple and straightforward to implement in a code. In chapter 3, we will see that the equation for LBM is very similar to LGCA, since LBM uses the same concept. However, LGCA has some serious drawbacks due to its boolean representation (Succi, 2001): lack of galilean invariance, statistical noise, exponential complexity, spurious invariants, etc.

LBM is a floating-point counter-part of LGCA that is able to cure these drawbacks. For this reason, LBM is a preferred fluid flow simulation method over LGCA.

Third, the lattice system in LBM allows a direct simulation in a digital pore image. This way, the pore geometry can be preserved. As high-resolution images of a pore structure and high performance computing become more available nowadays, LBM is becoming a powerful method. In addition, LBM is well suited for parallel computation, therefore enables faster simulation.

This document is made as a requirement for "TPG4920 - Petroleum Engineering, Master Thesis" course. This thesis is a continuation to the "TPG4560 - Petroleum Engineering, Specialization Project", where fundamentals of LBM: Cellular Automata and Boltzmann Equation are discussed. Then, a simple code was developed and was compared to the classical fluid dynamics result. The study shows that LBM is able to reproduce the analytical solution, and is able to produce some flow characteristics, e.g. turbulence. Other studies have shown that LBM can reproduce other fluid flow models: flow around a cylinder (Higuera and Succi, 1989; Grucelski and Pozorski, 2013), lid-driven cavity (Hou et al., 1995; Luo et al., 2011; Pradipto and Purqon, 2017), capillary rise (Sukop and Thorne Jr., 2006), and two-phase flow in a capillary tube (Leclaire et al., 2017).

In this thesis, we are interested in the modeling of two-phase flow in a realistic pore structure extracted from a microfluidic chip. As in any other fluid dynamic methods, modeling of multi-phase flow is not trivial; the approach requires assumptions and approximations to a certain extent. Therefore, one important research question is whether LBM is able to reproduce a typical fluid displacement mechanism in a pore structure.

1.1 Objective

In NTNU reservoir lab, we are conducting microfluidic flooding experiments to observe pore-scale displacement mechanisms. While there have been an extensive number of experimental studies, there exists few simulation studies. One can benefit from the simulation studies by having flexibility over the fluid and pore structure model, especially using LBM. In addition, the information gathered from the experiment is limited: we have fewer information about what is being done. On the other hand, in addition to the information from the experiment, simulation can give a much detailed information about the model e.g., we have access to the numerical data of each grid cells. Therefore, we can observe the first-order effect of the model. The main drawback of the simulation part is whether the results are representative. To check whether it is representative, one needs to compare the simulation result with an existing data: experimental result, for example. Thus, if we are able to reproduce experimental result in the simulation, we will have a more fundamental understanding of what is happening. As explained in following chapters, LBM has several features that can potentially reproduce microfluidic flooding experiments. This background motivates this thesis. For this reason, the thesis has objectives as follows:

- To understand the concepts of the lattice-Boltzmann modeling

- To understand the concepts of the pore-scale displacement mechanism
- To simulate a two-phase flow in a realistic pore structure extracted from microfluidic chip using lattice-Boltzmann modeling
- To observe the typical displacement mechanism, especially during primary drainage, in the simulations.
- To obtain two-phase flow properties from the simulation.

1.2 Sections

This thesis consists of several chapters: the first chapter contains a brief explanation of the thesis, including thesis background, objectives, and contents. The next two chapters are literature studies. In the second chapter, we review the fundamentals of wettability, interfacial tension, and capillary pressure. Additionally, we also go through the typical fluid displacement mechanisms at the pore scale for both drainage and imbibition processes. In the third chapter, we discuss about the lattice system, the governing LBM equation, the boundary condition, the implementation for multi-phase flow, and the unit conversion.

In the fourth chapter, the simulation setup is elaborated in detail, especially the pore structure and the LBM parameters. Further, the LBPM software is also introduced. In the next chapter, the simulation results are discussed. We simulate droplet case and micromodel case. In the micromodel case, the section is divided into parts, each with different LBM parameter change. The theory and the discussion are then summarized in the next chapter. Finally, in the last chapter, we put some recommendation for further study. Appendices are presented mainly for the derivation of the mathematics behind LBM.

Chapter 2

Fluid displacement in porous and permeable media

In this chapter, basic concepts regarding the fluid dynamics in porous media will be discussed. The focus is to present the typical displacement mechanism of multi-phase flow in porous media. The chapter will begin with a brief discussion about wettability, interfacial tension, and the Young-Laplace equation. Then, the discussion continues with the types of displacement mechanism, especially at pore-scale level, and what are the deciding factors.

2.1 Wettability, interfacial tension, and the Young-Laplace equation

2.1.1 Wettability

When multiple phases (fluids) are present in the rock, each fluid are either classified as a wetting phase, or a non-wetting phase, based on their relative intermolecular attraction towards the rock surface. In general, rock surface has a strong intermolecular energy, and therefore prefers a fluid that is able to lower this energy. The fluid is classified as a wetting phase if the fluid tend to reside at the rock surface as compared to the non-wetting phase, and vice versa. The wettability of the rock surface can be observed by the contact angle formed by the presence of two fluids in contact with the rock surface. An example of this is illustrated in Figure 2.1, where a droplet of water is in contact with a solid surface and air. The angle is measured from the denser fluid (in this case, water). In an extreme case where the contact angle $\theta = 0$, the rock surface is completely water-wet. In this case, the water completely coat the rock surface. On the other hand, when $\theta = \pi$, the rock surface is completely air-wet.

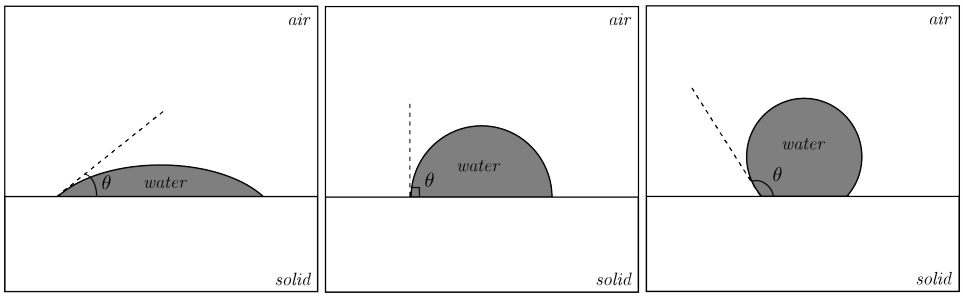

Figure 2.1: Water droplet on a solid surface with different contact angle in air-water system. **Left**: the solid surface is water-wet ($\theta < \pi/2$). **Center**: the solid surface is neutrally-wet ($\theta = 0$). **Right**: the solid surface is air-wet ($\theta > \pi/2$).

In a water-oil system reservoir, knowing the wettability of the reservoir rock is essential. We would expect higher oil recovery in a water-wet rock than in an oil-wet rock, since the water in water-wet rock resides on the rock surface and therefore the oil can mobilize easily inside the pore. On the contrary, we would expect lower oil recovery in an oil-wet rock than in a water-wet rock, since the water in water-wet rock is repelled from the rock surface and the oil tends to reside on the rock surface.

2.1.2 Interfacial tension

Interfacial tension is the energy per unit area of the surface between the phases, or the change in free energy for a change in interfacial area (Blunt, 2017). This quantity is large when one of the phases has a strong intermolecular bonding, and weak when both phase have similar intermolecular bonding. The interphase between the phase is such that the surface energy between of the system is minimum. In a general two-phase system, we have three interphases of interest:

1.) Non-wetting and wetting phase, γ_{nw}

2.) Non-wetting phase and solid, γ_{ns}

3.) Wetting phase and solid, γ_{ws}

Using force balance in horizontal direction (see Figure 2.2), one can find the relationship between these parameters:

$$\gamma_{ns} = \gamma_{ws} + \gamma_{nw} \cos\theta \tag{2.1}$$

where θ is the contact angle formed between the phases as explained in the previous subsection. This relationship can also be proved by observing the energy conservation of a droplet of fluid with constant volume.

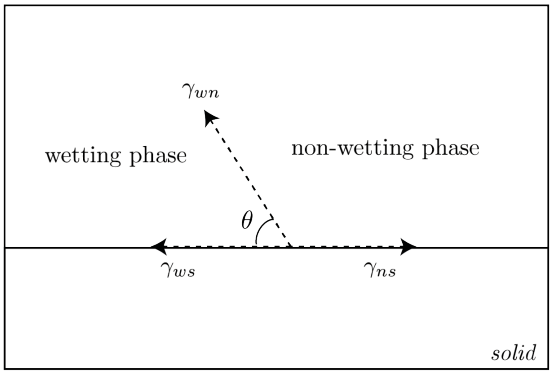

Figure 2.2: Force balance at fluid interphase (modified from Blunt (2017)).

2.1.3 Young-Laplace Equation

At the fluid interface, there are a pressure difference between the two phases. This pressure difference is compensated by the surface area change due to interfacial tension as:

$$(P_{nw} - P_w)dV = \gamma dA \tag{2.2}$$

where P_{nw} and P_w is the pressure of the non-wetting fluid and wetting fluid, respectively. The difference in pressure is defined as the *capillary pressure*, $P_c = P_{nw} - P_w$. The differential dV and dA depicts the change in volume of non-wetting phase relative to wetting phase, and the change in surface area, respectively. These parameters are dependent on the geometry of the fluids. If the form of the geometry is a sphere of radius r, we will have $dV = 4\pi r^2 dr$ and $dA = 8\pi r dr$, therefore:

$$P_c^{sphere} = \frac{2\gamma}{r} \tag{2.3}$$

In general, the geometry of the fluids is such that it has different principal radii of curvature in many directions. Let r_1 and r_2 be the maximum and the minimum principal radii of a general geometry, the capillary pressure can then be defined as:

$$P_c = \gamma\left(\frac{1}{r_1} + \frac{1}{r_2}\right) = \kappa\gamma \tag{2.4}$$

where κ is called the total curvature. Every location in a pore structure has its corresponding curvature. Therefore, based on Equation 2.4, we can predict the fluid distribution in

a pore structure. Consider the difference in curvature of two pore throats with different size. In a bigger size pore throat, the total curvature is smaller compared to the smaller pore throat. As a consequence, the capillary pressure in a bigger size pore throat is also smaller (Here, we assume that the interfacial tension is uniform across the pore structure) compared to the capillary pressure in a smaller pore throat. This means that the fluid displacement occurs easier when the pore throat size is bigger.

2.2 Fluid Displacement

There are two main fluid displacement types in porous media: drainage and imbibition. They are distinguished based on which phase is displacing, and which phase is being displaced. In this part, we are interested in observing the physical displacement mechanism at the pore scale. Lenormand (1999) observed two main type of pore-scale displacement mechanism: a) *pore invasion*, where the fluid displacement is due to the change in capillary pressure which then affect the radius of curvature. b) *collapse in a channel*, when one phase displace another, there is a critical pressure at the pore throat in which the non-wetting fluid becomes discontinuous. In both cases, we assume that the flow is induced by either viscous or capillary pressure drop only. Details about these mechanisms are elaborated in the following sections.

2.2.1 Primary Drainage

A drainage process is when a porous rock is initially saturated with a wetting phase, then a non-wetting phase is introduced to the rock. The non-wetting phase then displace the wetting phase. The term 'primary' is used to suggest that the rock is initially fully saturated with the wetting phase. An example of such phenomena is during the secondary migration. The reservoir is initially filled with water (the wetting phase), then invasion of oil or gas (the non-wetting phase) from the source rock occurs. The water is displaced and the oil or gas is accumulated in the reservoir.

The *macroscopic* capillary pressure is described as a function of water saturation. As the non-wetting fluid invades, the wetting saturation decreases and the capillary pressure increases. There is a threshold pressure, $P_c^{threshold}$, where the non-wetting fluid is first able to invade through the pore structure. This pressure corresponds to the invasion of the non-wetting fluid to the largest throats adjacent to the fluid interface. As the capillary pressure increases, one can measure the capillary pressure as a function of the wetting phase saturation across the pore structure. There is an asymptote when the saturation approaches the critical wetting phase saturation. This value depicts the volume of water trapped within a very small pore, in which the non-wetting phase cannot invade further. Using Equation 2.4, by knowing the interfacial tension between the fluid phases, each capillary pressure value corresponds to a curvature. Therefore, the measured capillary pressure can explain the curvature (and thereby the pore-size) distribution of a pore structure.

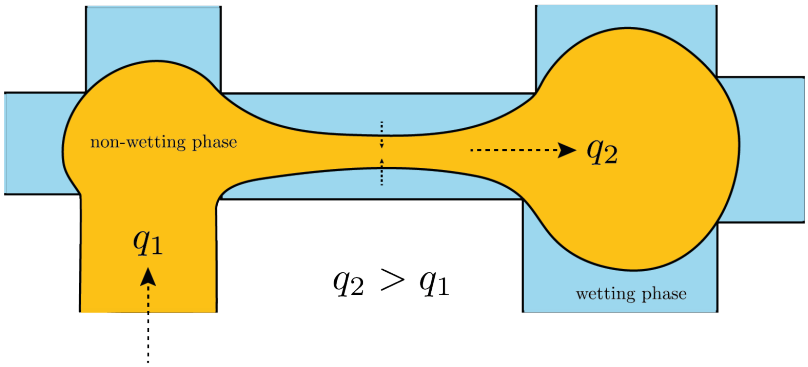

Figure 2.3: Snap-off during drainage process. Modified from Lenormand et al. (1983).

Since the non-wetting fluid has access to more of the pore structure when the capillary pressure increases, the non-wetting fluid might invade a bigger pore sizes that corresponds to smaller capillary pressure. This causes a flow from a locally higher capillary pressure to this location. This phenomena is called *Haines jump*. This is described as a jump of fluid from the locally smaller pore to the bigger pore. Further, the displacement at the pore throat is only at the center of the throat since the edges usually retain the wetting-phase. If the fluid supply from the locally higher capillary pressure part of the pore is not sufficient, then the non-wetting phase will separate itself from the continuous part. This is due to the creation of unstable filament when the non-wetting fluid is no longer in contact with the grain at the pore-throat (Lenormand et al., 1983). The non-wetting phase then *snap-off* and form a ganglion (see Figure 2.3).

Lenormand (1999) identified three main flow regimes for drainage phenomena (see Figure 2.4), depending on the capillary number and the viscosity ratio of the two fluids:

- *Capillary fingering*. Viscous forces are negligible in both fluids since the injection rate is very low.
- *Stable displacement*. When the flow rate is high and the capillary forces is low in the wetting phase (small mobility ratio).
- *Unstable displacement*. When the pressure drop is negligible in the non-wetting phase (high mobility ratio)

Generally, the non-wetting phase does not displace the entire wetting phase. Not only due to the bypassed wetting phase as in the case of the unstable displacement, for instance, but the remaining wetting phase is kept in the cracks, crevices, or the corners of the pore space. This remaining wetting phase is denoted as wetting layers. The wetting layers are of macroscopic thickness, have bulk or close-to-bulk properties, and do allow flow, albeit slow flow, over reasonable time scales (Blunt, 2017).

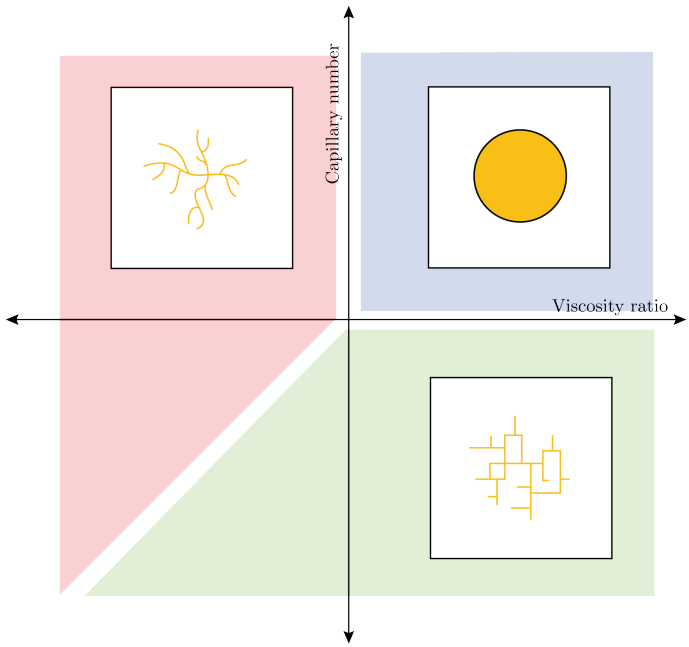

Figure 2.4: Phase diagram for drainage based on the capillary number and viscosity ratio. Non-wetting fluid is injected in the middle. Modified from Lenormand (1999). In this figure, each color corresponds to a flow regime: **Red**: unstable displacement, **Blue**: stable displacement, and **Green**: capillary fingering.

2.2.2 Imbibition and trapping

An imbibition process is when the wetting phase displace the non-wetting phase. In the context of an oil reservoir, this can be a process of waterflooding, where water (wetting phase) is injected in order to displace the oil (non-wetting phase). In this particular case, the reservoir initial condition is partially saturated with water, as a result of primary drainage. At a certain height above the water-oil contact, the reservoir is at the saturation where the water saturation is at S_{wc}. In this condition, the majority of the pore space contains the non-wetting phase as its continuous phase, while the crevices, cracks, and corners will be filled with the wetting phase. These layers of wetting phase is assumed to be connected.

In imbibition, the capillary pressure decreases over time as the wetting phase is introduced into the system. If only flow in the wetting layer is assumed, then these water layers will swell. The swelling process is most significant at the pore throat, especially at the narrowest path. The swelling continues until the wetting phase fills the pore throat, and therefore *pinch-off*[1] the non-wetting phase. Then, the fluid interface after *pinch-off* will move to the next narrowest part of the throat and eventually fills the center of the pore body. Thus, the flow regime during imbibition process is highly dependent on the pore geometry.

The other displacement mechanism is piston-like throat filling. This only happens at a high flow rate. As the wetting fluid is injected, the fluid interface moves through the pore throat. As the interface moves towards a pore body, only at a certain capillary pressure value that the interface can fill move through the center of the pore. This is the threshold capillary pressure, which corresponds to the largest radius of curvature of that pore body.

The displacement mechanisms in imbibition are more complex than drainage. Therefore, it is common to describe them in a simple model. Lenormand et al. (1983) used a pore network model and divided the imbibition mechanism into two types: *Imbibition I1* and *Imbibition I2* (see Figure 2.5). While observing the fluid interfaces through a pore body with four ducts the difference is whether the non-wetting fluid is initially is in one duct or two ducts. In both cases, the idea is similar: As the wetting-phase pressure increases, the fluid interface approaches the pore body. When it reaches the pore body, instability occurs since the meniscus is no longer in contact with the walls. This leads to a higher fluid curvature that corresponds to a lower capillary pressure. Therefore, the pore filling occurs rapidly.

The imbibition process can also be divided into two parts depending on the aspect ratio, or ratio of pore-to-throat size (Lenormand et al., 1983).

1) Large aspect ratio. In this case, the wetting fluid displaces the non-wetting fluid by means of series of pinch-off at the pore throats.

[1]The term *snap-off* and *pinch-off* are used interchangeably in different literature. Both terms describes the process when the non-wetting fluid become discontinuous. For clarity, we have used the term *snap-off* as the mechanism in drainage and *pinch-off* as the mechanism in imbibition. Other term usually used in this context is collapse.

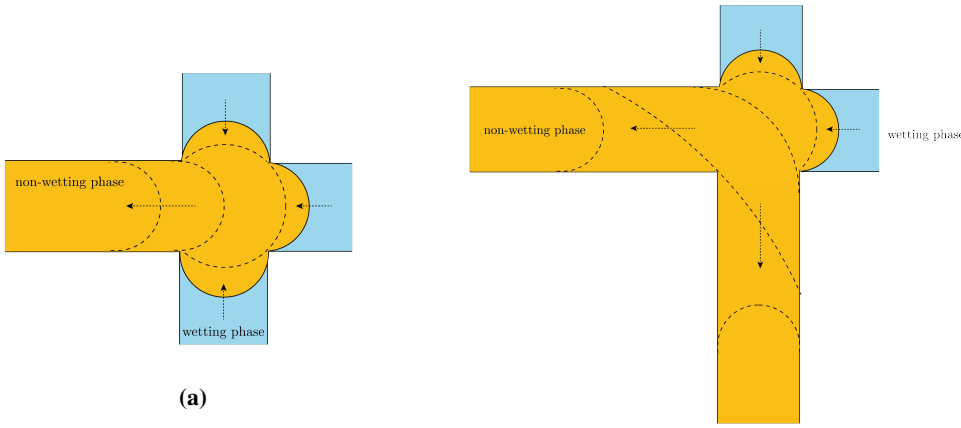

Figure 2.5: Imbibition type configuration in a pore network by Lenormand et al. (1983). a) Imbibition I1 and b) Imbibition I2.

2) Small aspect ratio. In this case, the network filling is characterized by a faceted crystal.

The illustration in Figure 2.6 are examples of extreme cases, the real pore structure has an intermediate pore-to-throat size.

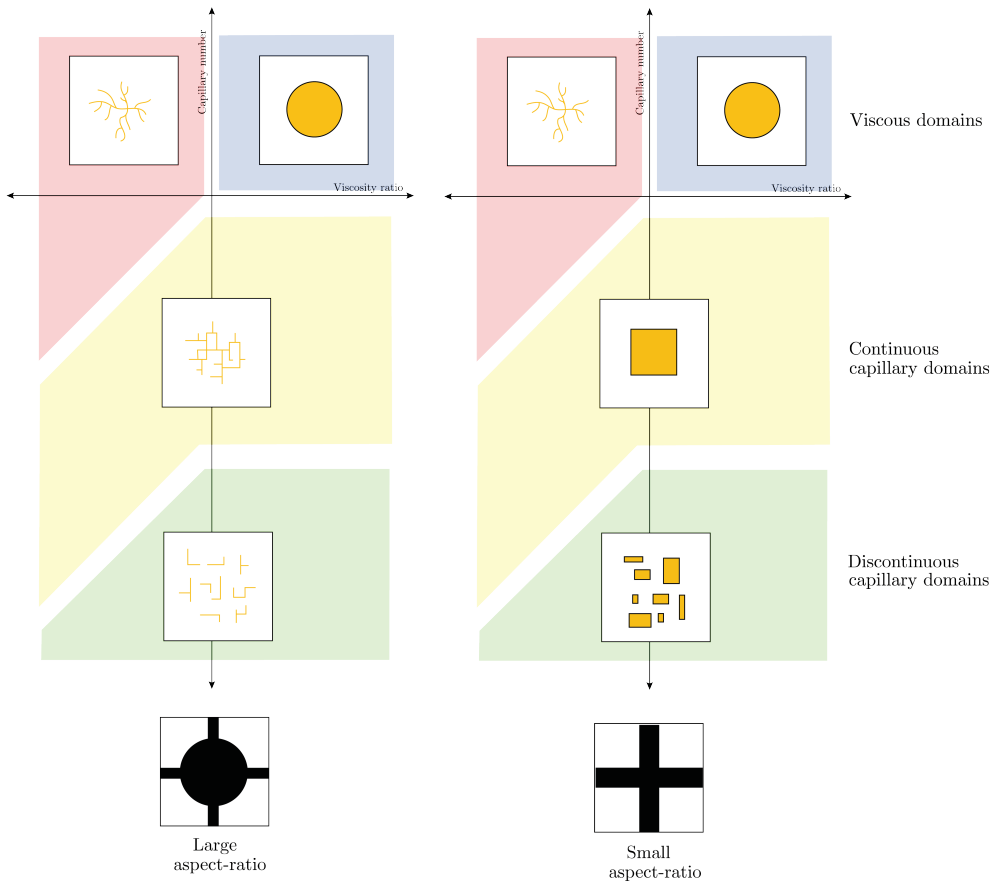

Figure 2.6: Phase diagram for imbibition. Wetting fluid is injected in the middle. Modifed from Lenormand (1999). In this phase diagram, the flow regime is further divided based on the aspect-ratio of the pore structure.

Chapter 3

Lattice Boltzmann Modeling

There are two types of pore-scale simulation: pore network modeling and lattice Boltzmann method. In pore network modeling, the pore space is commonly represented by a network of spheres (pore bodies) and tubes (pore throats). The extraction of pore network from the realistic pore structure has to conserve the topology of the pore space, and the distribution of the geometrical shapes and sizes. The fluid flow is then modeled using invasion percolation theory. Since the model is idealized, the computational power is less demanding.

The focus of this thesis is to model the fluid flow in porous media by using LBM. This method observes the fluid flow at particle level and therefore is able to produce the flow at pore-scale level. With the vast amount of particles in a fluid system, it is necessary to describe the particles in terms of distribution. As opposed to pore network modeling, a realistic pore structure can be directly used in this method. Since the objective of the thesis is to compare the simulation at pore-scale with experimental results, where pore geometry is important, this method is preferred. However, the downside of this method is that it is more computationally demanding.

Qian et al. (1992) introduced the $DnQm$ system where n is the system dimension and m is the number of possible momentum direction of the particles. The distance between lattice is set to 1 lattice units (1 lu) and the time step is set to 1 time step (1 ts). The microscopic velocity for each direction is therefore 1 lattice unit per time step (1 lu/ts). For instance, in $D2Q9$ system (see Figure 3.1), the velocity is defined as follows:

$$\vec{c}_a = \left\{ \begin{array}{ll} (0,0), & \text{for } a = 0 \\ (1,0),(0,1),(-1,0),(0,-1) & \text{for } a = 1,2,3,4 \\ (1,1),(-1,1),(-1,-1),(1,-1), & \text{for } a = 5,6,7,8 \end{array} \right\}$$

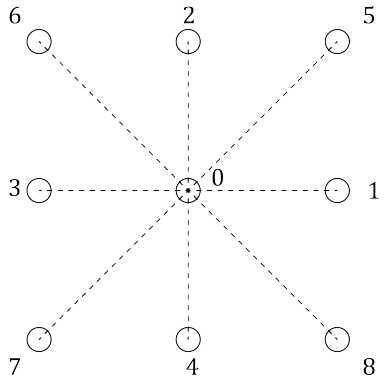

Figure 3.1: D2Q9 LBM model. The numbers corresponds to index of the velocity directions, denoted as a.

3.1 Basic equations

Let $f(\vec{x}, t)$ be the distribution function of particles that reside at position $\vec{x}$ at time t. In the original definition in Boltzmann Equation, the function is also described by its microscopic velocities, $f(\vec{x}, \vec{c}, t)$. In LBM, however, the microscopic velocity is discretized. Therefore, the particle distribution function, $f(\vec{x}, t)$, is a set of density functions $f_a(\vec{x}, t)$. The particle distribution in LBM undergoes two processes: streaming and collision. The streaming part depicts the movement of the particle distribution from a lattice to the neighboring lattice. In this case, the particle distribution will move to another the neighboring lattice position with a velocity of c_a. At the next time step, the next position will then be $\vec{x} + \Delta\vec{x} = \vec{x} + \vec{c}_a \delta t$. At the same time the particle distribution are being sent out to the neighboring lattice, the lattice also receives particle distribution from the neighboring lattice. This incoming particle distribution then collides, and relax towards local equilibrium (see Figure 3.2). The process continues with the same fashion until the system relaxes into a global equilibrium.

Following the general Boltzmann equation (see Appendix A for the derivation of this equation), the governing equation to the lattice Boltzmann equation is expressed as follows:

$$\left|f_a(\vec{x}, t)\right\rangle - \left|f_a(\vec{x} + \vec{c}\delta t, t + \delta t)\right\rangle = \frac{1}{\tau}(\left|f_a(\vec{x}, t)\right\rangle - \left|f_a^{eq}(\vec{x}, t)\right\rangle) \tag{3.1}$$

where $a = 0, 1, 2, \ldots, m-1$ denotes the index of the direction, as illustrated in Figure 3.1 and Figure 3.3 for $D2Q9$ and $D3Q19$ model, respectively. The l.h.s. of the equation is the streaming part and the r.h.s. is the collision part of the LBM. The collision part in this formulation is called BGK approximation, as proposed by Bhatnagar et al. (1954). The approximation depicts the relaxation of the distribution towards local equilibrium with a characteristic time, τ. This relaxation formulation is one of many possible ways to model

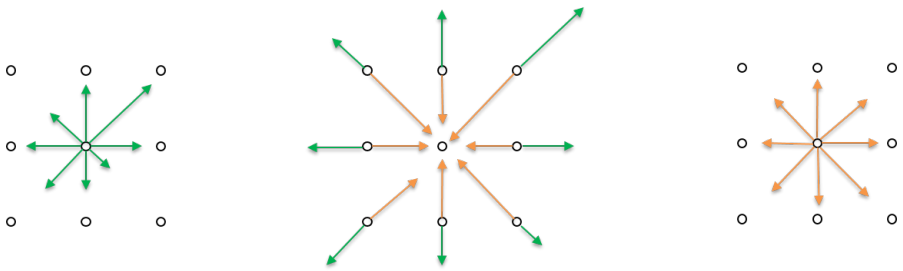

Figure 3.2: Illustration of streaming and collision process in LBM. Distribution functions are depicted as arrows. **Left**: pre-streaming. Green arrows (initial distribution functions) occupy the lattice. **Center**: streaming (receiving) and collision. The lattice sends the green arrows to the neighboring lattice and receive the orange arrows. The orange arrows then collide in the lattice. **Right**: post-collision. After the collision, the distribution relax towards equilibrium, and ready to move to the neighboring lattice in the next time step.

the relaxation process, but this is often used due to its simplicity.

In LBM, we can calculate the macroscopic parameter such as lattice fluid density, $\rho(\vec{x})$, and macroscopic velocity, $\vec{u}(\vec{x})$, at position $\vec{x}$. The lattice fluid density is calculated as the sum of all the particle density functions in the lattice:

$$\rho(\vec{x}) = \rho_0 \sum_a f_a(\vec{x}, t) \tag{3.2}$$

where ρ_0 is an arbitrary scalar factor. The lattice macroscopic velocity is calculated by adding all the product of the microscopic velocity and the corresponding distribution function at the lattice:

$$\vec{u}(\vec{x}) = \frac{1}{\rho(\vec{x})} \sum_a \vec{c_a} f_a \tag{3.3}$$

In the presence of an external force $\vec{F}$, the velocity is increased proportional to the mass and the relaxation time τ. Thus, the velocity at equilibrium can be calculated as follows (Sukop and Thorne Jr., 2006):

$$\vec{u}^{eq} = \vec{u} + \Delta\vec{u}_{ex} = \vec{u} + \frac{\tau\vec{F}}{\rho} \tag{3.4}$$

The relaxation time τ from Equation 3.1 can be related to the kinematic viscosity (ν) of

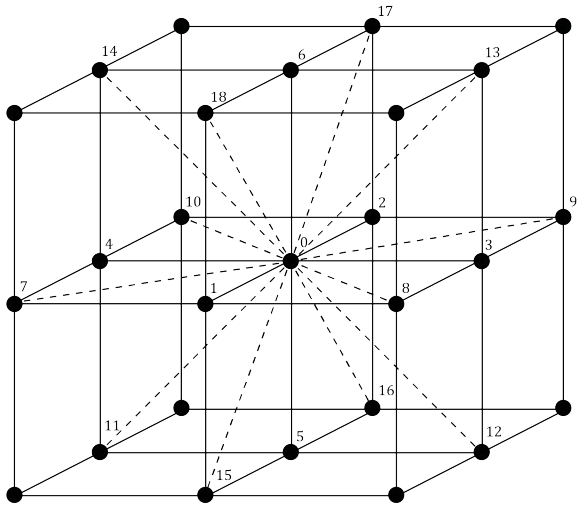

Figure 3.3: D3Q19 LBM model.

the fluid by the Chapman-Enskog expansion:

$$\nu = c_s^2\left(\tau - \frac{1}{2}\right) \tag{3.5}$$

where c_s is the speed of sound. Since the value ν has to be positive, it leads to $\tau > \frac{1}{2}$. The equilibrium distribution term in Equation 3.1 is calculated by approximating the Maxwellian distribution with third-order Gaussian-Hermite quadrature (Zou and He, 1997). It is computed as follows:

$$f_a^{eq}(\vec{x},\vec{u}) \approx \rho(\vec{x})\omega_a\left[1 + 3\frac{\vec{c}_a\cdot\vec{u}}{c_s^2} + \frac{9}{2}\frac{(\vec{c}_a\cdot\vec{u})^2}{c_s^4} - \frac{3}{2}\frac{\vec{u}^2}{c_s^2}\right] \tag{3.6}$$

where ω_a is the weight factor that corresponds to direction a. The derivation of this equation is shown on Appendix B. Appendix C shows the derivation to obtain the value of the weight factor.

3.2 Boundary Condition

In the previous section, the main part of LBM is discussed. In this part, boundary condition is discussed. Boundary condition is essential to resemble the actual fluid flow, however it can also be used to simplify the simulation. An example of such simple simulation is

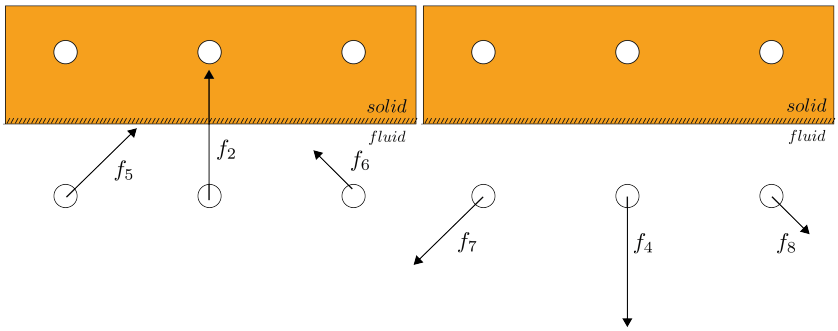

Figure 3.4: Illustration of bounce-back scheme in a no-slip boundary condition. **Left**: pre-stream. **Right**: post-stream.

when using a periodic boundary. In a periodic boundary, there is no boundary: the end of a grid structure is directly connected with the opposite end of the same grid structure. This results in the periodic topological spatial domain, e.g. cylindrical or torous topology. Periodic boundary condition allows the simulation to be run using the main part of LBM as is (provided no other boundary condition is applied).

However, in fluid flow simulation that resemble real condition, we usually need the other two types of boundary condition: solid-fluid boundary condition and inlet-outlet boundary condition. For solid-fluid boundary condition, a no-slip boundary condition is the most common boundary condition that is used.

In a no-slip boundary condition, the fluid velocity at the boundary is zero. In LBM, this is done by assuming that the bounce-back scheme holds in the direction towards the solid lattice. The bounce-back scheme is when the distribution function is rebounded into the opposite direction in the next time step, with the same magnitude (see Figure 3.4).

The idea behind the bounce-back scheme is to cancel the incoming momentum. Therefore, to accurately depict zero velocity in the boundary, one has to put the boundary exactly half-way between two lattice points. This limitation becomes a problem when complex pore-structure is encountered. To solve this problem, the pore structure resolution has to be high enough to capture the local physics and conservation rules (Ramstad et al., 2019). Additionally, one can use the improved method, e.g. interpolated bounce-back scheme and multi-reflection boundary conditions.

For inlet-outlet boundary conditions, the most common types are constant pressure and constant velocity boundary condition. To model this, Zou and He (1997) proposed the method where the distribution function is repopulated by imposing the required density or velocity at the lattice. For instance, for velocity boundary condition, given the velocity of $\vec{u}$ and the incoming distribution function at lattice, one can compute the velocity and the remaining distribution function. The relationship is as follows:

$$\rho = \frac{1}{1+u_\alpha}[\sum_i f_i + 2\sum_j f_j] \tag{3.7}$$

where α is one of the base direction, i is the direction perpendicular to α and rest particle in which the distribution function is known, j is the remaining direction in which the distribution function is known. The unknown distribution then can be solved by assuming that the bounce-back boundary condition holds for the distribution parallel to the flow direction. Note that Equation 3.7 can be rearranged such that in a pressure boundary condition case, given the density ρ, the required velocity can be computed.

3.3 Multiphase LBM

3.3.1 Colour gradient method

The colour gradient method is one of the method to model immiscible fluids in LBM. This method was first introduced by K. Gunstensen et al. (1991). In this method, a perturbation is added to the collision operator. This perturbation depicts attraction between the similar phase and the repulsion between different phases, creating interface between phase. The perturbation is a function of the density gradient between the fluid phases. For two phase flow, the phases are named as "Red" and "Blue" with their corresponding particle distribution f_a^R and f_a^B, respectively.

Observe the modified lattice Boltzmann equation:

$$\left|f_a(\vec{x}+\Delta\vec{x}, t+\Delta t)\right\rangle = \left|f_a(\vec{x},t)\right\rangle + \left|\Omega_a(\vec{x},t)\right\rangle + \left|S_a(\vec{x},t)\right\rangle \tag{3.8}$$

where Ω_a is the collision term and S_a is the source term depicting external force. In colour gradient method, the external force is the previously mentioned perturbation. The model is proposed by Grunau et al. (1993). In the absence of other external force, it is in the form of:

$$S_a' = A|g|\left(w_a \frac{(\vec{c}_a \cdot \vec{g})^2}{|\vec{g}|^2} - B_a\right) \tag{3.9}$$

where A and B are tunable parameters. The parameter A is proportionally related to the surface tension. The local color gradient $\vec{g}$ is defined as:

$$g(\vec{x}) = \sum_a \vec{c}_a[\rho_R(\vec{x} + \vec{c}_a) - \rho_B(\vec{x} + \vec{c}_a)] \tag{3.10}$$

Notice that g is small in incompressible, homogeneous lattice, and is large near the interface between the fluids. After the perturbation, the next step is to recolor the mass. This process is done by solving the following maximization problem:

$$W = \max_{f^{R*}, f^{B*}} \left[\sum_a \vec{c}_a (f_a^{R*} - f_a^{B*}) \right] \tag{3.11}$$

The solution must be constrained to conservation of red fluid mass, blue fluid mass, and the total mass in each lattice direction. Mathematically, these constraints can be expressed as follows:

$$\sum_a f_a^{R*} = f_T^R \tag{3.12}$$

$$\sum_a f_a^{B*} = f_T^B \tag{3.13}$$

$$f_a^{R*} + f_a^{B*} = f_a^* \tag{3.14}$$

where f_T^R and f_T^B are the total red mass and total blue mass before the collision, respectively. The drawback of colour gradient method is that the interface gets pinned to the lattice. This is due to insufficient velocity to move significant amount of phases to another site. To solve this problem, Latva-Kokko and Rothman (2005) proposed the improved redistribution of the fluid particles:

$$f_a^{R*} = \frac{\rho_R}{\rho} f_a^* + \beta \frac{\rho_R \rho_B}{\rho^2} f_a^{eq}|_{\vec{v}=0} \cos\phi \tag{3.15}$$

$$f_a^{B*} = \frac{\rho_B}{\rho} f_a^* - \beta \frac{\rho_R \rho_B}{\rho^2} f_a^{eq}|_{\vec{v}=0} \cos\phi \tag{3.16}$$

where β is the separation parameter, and taking any value between 0 and 1. If β increase, then the interface will be less diffuse. To conclude, the following are the steps to colour gradient method (K. Gunstensen et al., 1991):

1. Calculate the total distribution on each lattice $f_a = f_a^R + f_a^B$.
2. Calculate the average population density d, velocity $\vec{v}$, and equilibrium distribution f_a^{eq}

3. Calculate the single-phase collision, $f'_a = f_a + \Omega_a$

4. Add the perturbation effect due to surface tension to obtain f^*_a from f'_a, $f^*_a = f'_a + S_a$

5. Perform the recoloring to red and blue to obtain f^{R*}_a and f^{B*}_a.

6. Perform the streaming step such that $f^R_a(x + \Delta x, t + \Delta t) = f^{R*}_a(x, t)$ and $f^B_a(x + \Delta x, t + \Delta t) = f^{B*}_a(x, t)$

3.3.2 Inter particle potential method

In this thesis, inter particle potential method is not applied. However, this method is also commonly used other important LBM studies We will therefore present it for completeness. In this method, the separation between phases is incorporated into an attractive force $\vec{F}$ between nearest lattices. The attractive force is expressed as follows:

$$\vec{F} = -G\psi(\vec{x}, t) \sum \omega_a \psi(\vec{x} + \Delta x, t)\vec{c}_a \tag{3.17}$$

where G is the interaction strength and ω_i is similar to the weight factor in Equation 3.6. The interaction potential, ψ, is a monotonous and bounded function. Shan and Chen (1993) defined the interaction potential as:

$$\psi(\rho) = \psi_0 \exp\big(-\rho_0/\rho\big) \tag{3.18}$$

where ρ_0 and ψ_0 are arbitrary constants. The same idea can also be used to model the interaction between fluid particles and the solid surfaces. In this case, the "adsorption" force can be expressed as:

$$\vec{F}_{ads} = -G_{ads}\psi(\vec{x}, t) \sum \omega_a s(\vec{x} + \Delta x, t)\vec{c}_a \tag{3.19}$$

where s is one (1) if the lattice at location $\vec{x} + \Delta x$ is a solid and is zero (0) if it is not a solid. G_{ads} is the coefficient that represent the adsorption strength. Further, this parameter also allows different range of contact angles to be modeled. The weakness of this method is that only the attraction force is incorporated in the model, while the repulsive force is neglected. As a consequence, this model has a limitation to mimic the fluid EOS (Sukop and Thorne Jr., 2006).

3.4 Multiple relaxation time

The aforementioned BGK approximation is sometimes called as single-relaxation time approximation. This is because the whole collision process is represented in one characteristic time. This allows great simplification of the collision integral and therefore is commonly used.

Another method that is commonly used is multiple-relaxation time (MRT). The idea behind MRT is to solve the collision process in moment space $\mathbb{M}$. This method is first studied by D'Humières et al. (2002). The collision term on the rhs of Equation 3.1 is transformed with a group of base vectors ϕ_k, with $k = 0, 1, \ldots, N$ where N is the number of moments (equal amount to the discrete directions). These vectors are the results of Gram-Schmidt orthogonalisation of velocity polynomials with a set of velocities c_a and the corresponding distribution f_a. This results in the moment m_k:

$$m_k \equiv \langle \phi_k | f \rangle \,, \quad \langle f | = (f_0, f_1, \ldots f_N) \tag{3.20}$$

Now we define the matrix $M = |\phi_k\rangle_i$ such that the collision matrix $\Omega = M^{-1} \cdot \hat{\Omega} \cdot M$. In addition, $\{\phi_k\}$ are the eigenvectors of matrix Ω. Therefore:

$$\begin{aligned} \big|f_a(\vec{x},t)\big\rangle - \big|f_a(\vec{x}+\vec{c}\delta t, t+\delta t)\big\rangle &= \Omega(\big|f_a(\vec{x},t)\big\rangle - \big|f_a^{eq}(\vec{x},t)\big\rangle) \\ &= M^{-1}\cdot\hat{\Omega}\cdot M(\big|f_a(\vec{x},t)\big\rangle - \big|f_a^{eq}(\vec{x},t)\big\rangle) \\ &= M^{-1}\cdot\hat{\Omega}(\big|m_a(\vec{x},t)\big\rangle - \big|m_a^{eq}(\vec{x},t)\big\rangle) \end{aligned} \tag{3.21}$$

where $\hat{\Omega} \equiv \mathrm{diag}(s_0, s_1, \ldots, s_N)$ and s_k is the relaxation rate of moment k. The moments, m_k then can be divided into two groups based on its local conservation: hydrodynamic (conserved) and kinetic (non-conserved) moments. For conserved moments, $m_k^{eq} = m_k$. Therefore, the relaxation rate s_k for conserved moment is irrelevant by definition. For athermal fluids, the locally conserved moments are density ρ and momentum $\vec{j}$.

As opposed to BGK approximation to the collision integral, MRT offers a more flexible approach to the tuning parameters. In BGK approximation, the only tuning parameter available is the characteristic time, τ. This translates to a collision matrix Ω with eigenvalue of τ. As a consequence, the characteristic time, τ is dependent on other parameters: viscosity, distribution function, relaxation time, etc. Therefore, despite the simplicity of BGK approximation, the parameter is prone to instability of the model. In MRT, instead of having only one tuning parameter, we have a number of tuning parameters that corresponds to the number of direction in the lattice system. One major drawback of MRT is that one has to compute the inverse of matrix M, which can be computationally expensive.

3.5 Unit conversion from physical to lattice unit

From the previous section, we know that all the parameters in LBM are described in lattice unit. To use LBM to solve physical model, one has to convert the unit system from the physical unit to the lattice unit. This section elaborates how to use the information from the physical parameters and how to set up the simulation in order to obtain the required LBM parameter.

The idea behind the unit conversion is similar to the Buckingham Pi theorem: two equivalent systems must have the same dimensionless parameter. The two equivalent system would be the physical (P) and the lattice (LB) systems. To make the unit conversion easier, a dimensionless (D) system is introduced in between. In fluid flow, the most common dimensionless parameter is the Reynold Number (Re). The following relationship then must be satisfied:

$$Re_p = Re_d = Re_{lb} = \frac{lu}{\nu} \tag{3.22}$$

Suppose we have a system with a reference length $l_{p,0}$. Then the dimensionless length parameter l_d of any physical length l_p is defined as:

$$l_d = \frac{l_p}{l_{p,0}} \tag{3.23}$$

Similarly, we perform the similar definition to the time, and thus velocity:

$$t_d = \frac{t_p}{t_{p,0}} \tag{3.24}$$

$$u_d = \frac{u_p}{u_{p,0}} \tag{3.25}$$

For simplicity, we describe the dimensionless system as "the system in which $l_{d,0}$ and $t_{d,0}$ are unity". To start with the setup, the space discretization in LBM is such that the number of cells N_x used to discretize the space. We use the dimensionless reference length $l_{d,0}$, such that the space interval (or grid resolution) δ_x is defined as:

$$\delta_x = \frac{l_{d,0}}{N_x} = \frac{1}{N_x} \tag{3.26}$$

Similarly, the time interval δ_t of a simulation with a number of iteration N_t and dimen-

sionless reference length $t_{d,0}$ is

$$\delta_t = \frac{t_{d,0}}{N_t} = \frac{1}{N_t} \tag{3.27}$$

We can now define the lattice length l_{lb}, lattice time t_{lb}, and lattice velocity u_{lb} as

$$l_{lb} = N_x l_d = \frac{l_d}{\delta_x} \tag{3.28}$$

$$t_{lb} = N_t t_d = \frac{t_d}{\delta_t} \tag{3.29}$$

$$u_{lb} = \frac{N_x}{N_t} u_d = \frac{\delta_t}{\delta_x} u_d \tag{3.30}$$

Using above definitions, we also have a relationship for the dimensionless kinematic viscosity:

$$\nu_d = \frac{1}{Re} = \frac{\delta_x^2}{\delta_t} \nu_{lb} \tag{3.31}$$

where ν_{lb} is calculated from Equation 3.5 for a given relaxation time, τ. Notice that the LBM parameters do not only dependent on the physical parameter, but also on the resolution of the model. The choice of the resolution is mainly based on what level of detail that the simulation wants to capture. In the case of microfluidic simulation, we want to have high resolution in time and space to capture the displacement mechanism, such as Haines jump. However, resolution must be set in order to ensure stability. For example, we know that τ has to be larger than 0.5. If time resolution is too high, then τ will be very close to 0.5, leading to unstable simulation.

Chapter 4

Data and Methodology

4.1 LBPM

To simulate the LBM in the pore structure, this study uses an open-source software called LBPM. It is an acronym for Lattice Boltzmann for Porous Media. It is an open-source software developed by James McClure of Virginia Tech and is part of the Open Porous Media (OPM). It can be used to simulate a two-phase immiscible flow simulation with $D3Q19$ lattice system. It is built on C++ platform and utilizes parallel computation for the simulation. For these reasons, LBPM is an excellent software to use for the purpose of this thesis. LBPM is installed in seis.igp.ntnu.no, a Linux server with 20 cores and 132 GB memory.

The software contains several different solvers, each with different purposes. The ones that we are interested in are the pre-processing tools to prepare the simulation data, absolute permeability solver using LBM, and two-phase flow using colour-gradient LBM solver. The following subsections elaborates these solvers in further detail.

4.1.1 Grid decomposing

Before performing the LBM simulation, we first have to prepare the grid structure file such that it is readable by other solver. In addition, the grid structure must be decomposed into many separate subdomains for parallel computation. In LBPM, this is done by a pre-processor called `lbpm_serial_decomp`. This pre-processor reads the raw file of the pore structure, slices the domains into subdomains based on the desired number of processors in each direction, and setting up the boundary condition for two-phase flow simulation. The labels in the .raw file then is rewritten into the corresponding output labels to initialize the simulation.

Listing 4.1: "Domain" section of the input file

```
Domain {
    Filename = "pore04hr_resliced.raw"
    nproc = 4, 1, 4          // Number of processors (Npx,Npy,Npz)
    n = 200, 10, 200         // Size of local domain (Nx,Ny,Nz)
    N = 800, 10, 800         // size of the input image
    L = 7.5, 0.09375, 7.5    // Length of domain (x,y,z)
    BC = 4                   // Boundary condition type
    Sw = 0.20
    ReadType = "8bit"
    ReadValues = 0, 255      // labels in Filename
    WriteValues = 2, 0       // corresponding output labels
}
```

This pre-processor reads the "Domain" section of the input file. The output from this pre-processing step is subdomain files that will be used as an input for the other solvers.

4.1.2 Absolute permeability calculation

In LBPM, the `lbpm_permeability_simulator` solver is used to obtain the permeability of a grid structure. This solver performs a single-phase fluid flow to measure the permeability of the grid structure over time using LBM. The flow is induced by a body force in z-direction where periodic boundary condition is applied. This affects the fluid velocity inside the grid structure, as described in Equation 3.4. Instead, if one chooses to simulate by imposing external pressure boundary condition, one can specify the inlet and outlet density. On the other hand, if one chooses to simulate by imposing external flux boundary condition, one can specify the flux. In both cases, Equation 3.7 is used to compute the density function at the boundaries. The 'restart' value is set to 'false' to start a new simulation, or 'true' to continue from the latest saved time step.

Listing 4.2: "MRT" section of the input file

```
MRT {
    timestepMax = 100000     // maximum number of time steps to simulate
    tau = 0.7                // relaxation time
    F = 1.0e5, 0, 0          // external body force applied to the system
    Restart = false          // whether to restart from a checkpoint file
    din = 1.0                // density at inlet (if external BC is applied)
    dout = 1.0               // density at outlet (if external BC is applied)
    flux = 0.0               // volumetric flux in voxels per time step
}
```

This solver reads the "MRT" section of the input file, which consists of the input parameters to the single-phase LBM. MRT stands for multiple-relaxation-time (see section 3.4 for the theoretical background on this approach), which is performed in this solver. Here, all the relaxation parameters are different, but are dependent on τ.

4.1.3 Two-phase flow simulation

Finally, one can use `lbpm_color_simulator` to solve a two-phase flow simulation using LBM. This solver performs a two-phase fluid flow using colour gradient method

with various boundary condition. This is the main solver used in this thesis. The "Red" and "Blue" fluid is represented as fluid A and B in LBPM, respectively, where fluid A is the invading fluid and fluid B is the defending fluid. This solver reads the "Color" section of the input file, which consists of the input parameters to the two-phase LBM using colour gradient method.

Here, we specify the relaxation time and mass density for both fluid A and fluid B. The 'alpha' parameter in LBPM refers to A in Equation 3.9. The 'beta' parameter refers to β in Equation 3.15. We can also specify the wettability of each grain voxel by specifying the component affinity for each component's label. This part is useful when we have different wettability in our pore structure due to difference in mineral composition, for example. Since we are only using flux boundary condition, some parameters in this part are not needed as inputs: capillary number and target saturation.

Listing 4.3: "Color" section of the input file

```
Color {
    tauA = 0.5858;           // relaxation time for fluid A
    tauB = 0.53012;          // relaxation time for fluid B
    rhoA   = 1.0;            // mass density for fluid A
    rhoB   = 1.0;            // mass density for fluid B
    alpha = 1e 4;            // parameters correlated to the interfacial tension
    beta  = 0.95;            // parameters correlated to the interface width
    F = 0, 0, 0              // external body force applied to the system
    Restart = false          // whether to restart from a checkpoint file
    din = 1.0                // density at inlet (if external BC is applied)
    dout = 1.0               // density at outlet (if external BC is applied)
    timestepMax = 200000     // maximum number of time steps to simulate
    flux = 5.0               // volumetric flux in voxels per time step
    capillary_number = 1.0e 1    // capillary number for the system (if periodic
        BC is applied)
    ComponentLabels = 0          // list of solid mineral labels
    ComponentAffinity =  1.0     // list of mineral affinities
    target_saturation = 0.05, 0.10, 0.15, 0.25, 0.35, 0.45, 0.55, 0.60, 0.65
        // target saturation for morphological algorithm
}
```

The result of the simulation is stored by a .silo file for each subdomain. The output of this solver are the phase, pressure, and velocity of each voxel at each desired time step. The phase is the value that determines whether the voxel is completely fluid A (1), completely fluid B (-1), or an interface (otherwise). From here, one can observe the distribution of these parameters along the micromodel. One can refer to subsection 3.3.1 for all the theoretical calculation behind colour gradient method. This solver also has the 'restart' feature that can continue the simulation from the latest saved time step.

Notice that most of the numbers in the input file are numbers with lattice unit. Similarly, the output values are also described in lattice unit. Therefore, one has to compute the number from the physical unit to the lattice unit. To do so, refer to section 3.5. The only parameter with unit is the length of the domain, L in the "Domain" section. This is used to compute the permeability of the pore structure.

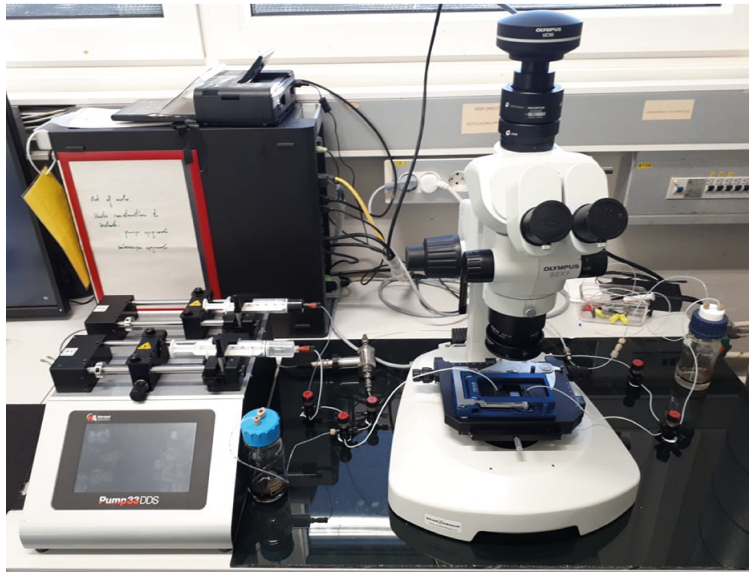

Figure 4.1: Microfluidic experiment setup.

4.2 Grid structure

As previously mentioned in the previous chapter, the digital pore image can be used directly as an input to LBM simulation. The digital pore image can be extracted from Micro-CT or Scanning electron microscopy (SEM) to get a realistic pore structure. We can also have a pore image generated synthetically, e.g. from sphere pack algorithm. In LBPM, the image is stored as a .raw file and is called in the "Domain" section of the input file.

In this thesis, the pore structure extracted from SEM image is used. The pore structure is then etched into a borosilicate chip. This chip is also sometimes called as microfluidic chip. The chip typically has a rectangular shape with a very small thickness. The chip we use has a size of 7.5 mm $\times$ 7.5 mm $\times$ 0.0935 mm. The reasoning behind using this structure is that the flooding study for microfluidic chip has been done extensively for experimental part, but there exist only a few studies for simulation. In the experiments, the fluid distribution can be recorded with a high-resolution, high frame-rates-per-second camera during the flooding. This allows direct comparison between the simulation and the experimental result. This part, however, is not part of this study and would be a good recommendation for further study.

Figure 4.1 shows the microfludic experimental setup. The fluid is injected by a syringe pump with a constant rate through a tiny tube. The tube is connected to a blue metal chip holder that contains the microfluidic chip. While the fluid is moving inside the chip, the camera start recording the picture. Eventually, the injected fluid pass through the outlet of the chip, which will then goes to a waste container.

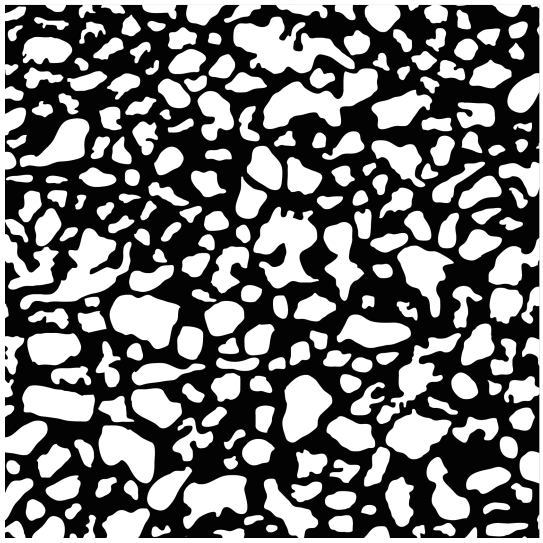

Figure 4.2: Image of the pore structure used in the simulation.

In this study, the digital pore image underwent two different processes: segmentation and grid refining. The grid structure is extracted from a thin-section of a sandstone (see Figure 4.2). The thin section is then segmented based on the pore space (0) and the grain (255). The segmentation is done with ImageJ™. Since the chip is essentially a stack of similar two-dimensional pore structure, the pore structure is adjusted to ensure connectivity from the inlet through the outlet. This leads to a higher porosity than a regular pore structure.

As mentioned in the previous part, high image resolution is required to avoid staircase error in the bounce-back implementation at the solid boundary. To obtain high resolution image with large coverage area, one has to improve the image resolution even further. The idea is to make a finer grid and assigning the value by interpolation. To do so, we use the software Adobe Illustrator™. The software traces pixel-based image and converts it to a vector-based image. There are several ways to do the conversion. From vector-based image, we can convert it back to the pixel-based image with the desired resolution. As a result, the region between fluid and solid might have intermediate value. To fix this, one can simply apply the segmentation process again.

The higher the resolution, the higher the computational cost of the simulation. In addition, higher resolution in the grid has to be compensated with higher resolution in time as well to ensure stability. This leads to an even higher computational cost. For this reason, one has to be aware of the required level of detail the simulation that one wants to obtain, as well as the computational capabilities of the computer.

Table 4.1: General setup for the LBM simulation.

Parameters	Symbols	Value
Time grid size	N_t	2000
Space grid size	N_x	800
Time interval	δ_x	0.0005
Space interval	δ_t	0.00125

Table 4.2: Reference physical parameters for the LBM simulation.

Parameters	Symbols	Value	Unit
Reference length	$l_{p,0}$	7.5	mm
Reference flux	$Q_{p,0}$	50	μL/min
Area	A	0.703125	mm^2
Reference speed	$u_{p,0}$	4266.67	mm/s
Reference time	$t_{p,0}$	0.001758	s

4.3 Simulation parameters

Prior to the microfluidic simulation, we are interested in seeing the effect of the wettability on the LBM simulation. The simplest way would be to simulate a water droplet on top of a solid surface and immersed in an oil tank, similar to Figure 2.1. This is done by observing the angle formed at the fluids contact with solid. In LBPM, the wettability is controlled by the component affinity parameter in the "Color" section. The component affinity is assigned to each solid identifier. It has a range of value between -1 to +1, where -1 corresponds to fluid B-wet solid and +1 corresponds to fluid A-wet solid.

To mimic the microfludic experiment, we are using the actual physical parameters used in the experiment e.g. chip size and fluid (oil and water) properties. Since the experiment is done with a constant flow rate, the simulation is also done in a similar way. We perform several simulations for sensitivity studies to capillary number (Ca), viscosity ratio (M), and wettability.

To implement it in LBM we need to convert the physical unit to lattice unit. The setup is shown in Table 4.1. The reason for choosing the space grid size, $N_x = 800$ is because the micromodel is segmented into 800 lattices in x-direction (also in y-direction). The time grid size, $N_t = 2000$ is purely set to satisfy the stability condition for LBM simulation.

Then, we define physical reference length and speed. The reference length is taken from the length of the micromodel, 7.5 mm. The reference speed is taken from the reference flux, 50 μL/min divided by the inlet area. These parameters are summarized in Table 4.2.

Chapter 5

Result and discussion

This chapter is dedicated for the simulation results and the discussion. We start with a droplet case to observe the effect of the component affinity to the wettability of the solid. The motivation behind this simulation is to distinguish the drainage and imbibition process later on.

The main simulation conducted here is the two-phase flow simulation using LBM in the micromodel, as described in the previous chapter. The simulation is conducted for both drainage and imbibition process. Here, the *drainage process* describes a process where the micromodel is water-wet and initially filled with water, while the invading fluid (oil) is injected into the system at a constant rate. On the other hand, the *imbibition process* is defined when the micromodel is oil-wet, while the fluids operating in the same manner as the drainage process simulation: the micromodel is initially filled with water and the oil is injected at a constant rate. Note that the drainage and imbibition process here are distinguished by the wettability of the micromodel only. This definition might differ from definitions used elsewhere, e.g. when describing capillary pressure hysterisis curves.

5.1 Droplet

Before conducting the two-phase simulation on the micromodel, we would like to investigate the effect of the component affinity on the wettability of the solid. In this case, a solid flat surface is assigned with a component affinity value, and the void space is filled with fluid B. Then a droplet of fluid A is introduced into the system. With a small body force, the droplet moves until it hits the flat surface. When it hits the surface, the droplet starts to interact with fluid B and the surface. When it reaches steady state, a contact angle is formed. From chapter 2, we know that the wettability of a solid can be indicated by the contact angle. Therefore, we can correlate between the component affinity and the rock wettability based on the contact angle formed in the simulation results.

The simulation is conducted with the following component affinities: -1.0, -0.5, 0.0, 0.5, and 1.0. The simulation results are shown in Figure 5.1. The figures display contour map of the fluid-A. In this case, the contour shows the interface between the two fluids. The contact angle is measured using a visualization tool available in an image editor. The figures show different contact angle formed with different component affinity. It turns out that the component affinity has a linear correlation with the contact angle (see Figure 5.2). However, we see a slight deviation when the component affinity is between 0 and 1.

Based on these results, we can expect to obtain the desired contact angle based on the linear correlation with the component affinity when component affinity is less than 0. On the other hand, we can expect the contact angle to be slightly deviatied from this linear correlation when component affinity is greater than 0. We must keep this in mind when we are going to run LBM simulation with with component affinity in this range. Further, we know from Equation 2.1 that contact angle can be correlated with the interfacial tension through a force balance. Rearranging the equation, and applying the linear correlation (for now, we assume linear correlation at all range of component affinity) between the two parameters, we now have:

$$\frac{\pi(\text{component affinity} + 1)}{2} = \theta = \cos^{-1}\left(\frac{\gamma_{ns} - \gamma_{ws}}{\gamma_{nw}}\right) \tag{5.1}$$

The equation above shows that the component affinity not only affects the contact angle, but also affects the difference in interfacial tension between fluids and solid, scaled by the interfacial tension between the two fluids. This means that for the same component affinity, if γ_{nw} is scaled with a factor k, then the difference in the fluid-solid interfacial tension, $\gamma_{ns} - \gamma_{ws}$ is also scaled with the same factor k. This is confirmed by running the same simulation by increasing the interfacial tension by an order of magnitude. The simulation results also shows the exact same contact angle for the same component affinity. This fact is important, since the component affinity is only set to the solid part of the simulation.

Equation 5.1 shows that the use of component affinity is a convenient way to describe the wettability of the solid. Instead of specifying the value for the interfacial tensions (fluid-solid and fluid-fluid) and calculating the contact angle, it specifies the contact angle first and then back calculate the interfacial tensions between fluids and solid (while the interfacial tension between the two fluids are given by other parameters). From Equation 5.1 we see that if the component affinity of the solid is < 0, then the solid is fluid-B wet. Similarly, if the component affinity of the solid is > 0, then the solid is fluid-A wet.

5.2 Micromodel

In this section, we will simulate a two-phase flow in a micromodel using LBM. The injected fluid is operated at a constant rate at the left side of the micromodel, and a constant pressure at the other side. This is conducted to mimic the micromodel simulation.

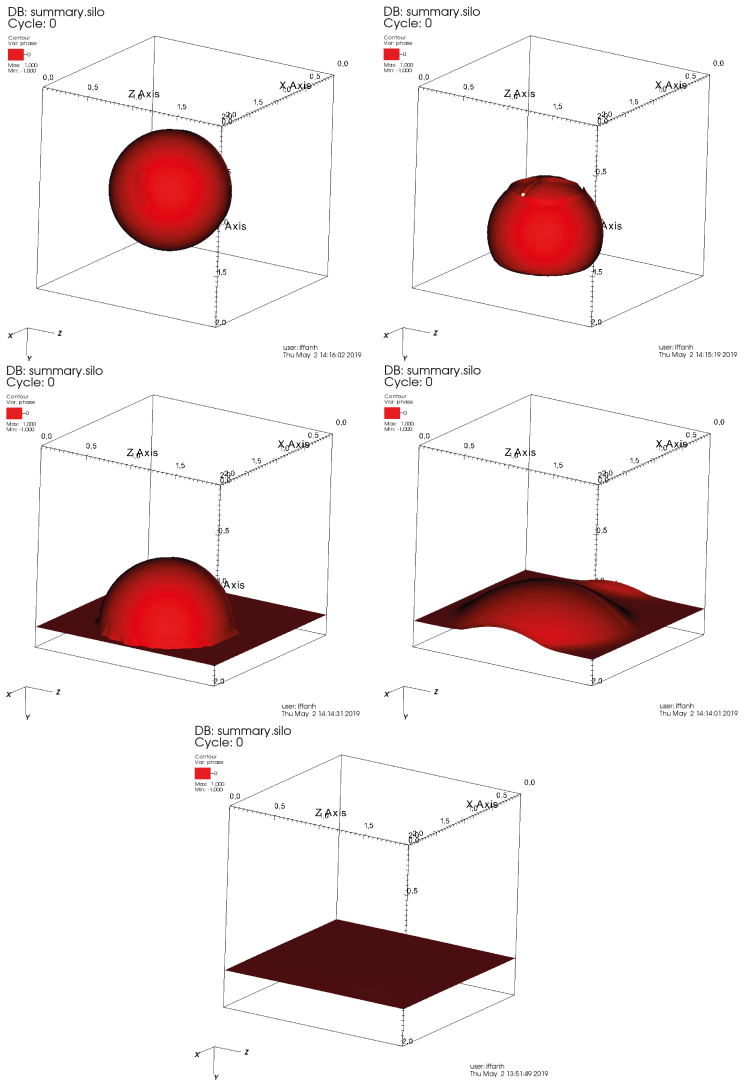

Figure 5.1: Droplet on a flat surface with a component affinity of **top left**: -1.0, **top right**: -0.5, **middle left**: 0.0, **middle right**: 0.5, and **bottom**: 1.0. The red contour shows the interface between the two fluids.

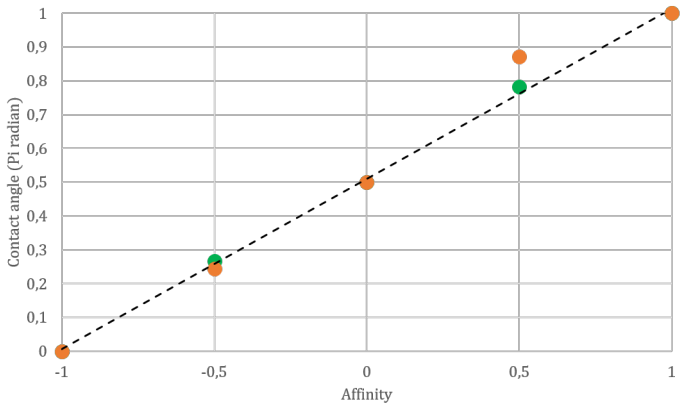

Figure 5.2: Correlation between affinity in LBM simulation and the resulting contact angle. The green dots represents the initial case and the orange dots represents the case with interfacial tension increased by an order of magnitude. There is a slight deviation when component affinity is between 0 and 1.

In the micromodel simulation, we have set the grid structure with the grid size of 800 $\times$ 800 $\times$ 10 (see Figure 4.2). Therefore, the voxel size is 7.5 mm$/800$ $=$ 9.375 μm. The domain was structured as 4 $\times$ 4 $\times$ 1 with 1 CPU per subdomain (16 CPUs in total).

5.2.1 Absolute permeability

First, we are interested in measuring the absolute permeability of the micromodel. To calculate the absolute permeability, we run the single-phase LBM on the micromodel (refer to subsection 4.1.2). The simulation is run with a body force in the $x-$direction. The simulation result is shown in Figure 5.3.

The figure shows a plot between measured permeability against the reciprocal of simulation time. We use the reciprocal of time to help visualizing the convergence better. Here, the converged value is obtained when the reciprocal of time approahces zero (corresponds to infinite time). As shown in the figure, the value of the permeability changes with simulation time, and eventually converges to a value. The converged value corresponds to the steady state condition in the LBM simulation. Permeability is initially measured at a higher value, because at the start of the simulation, the total average velocity is higher. During the simulation, the effect of the bounce-back boundary condition at the solid boundary results in lower velocity near the solid. In a complex pore structure, the effect might not be that clear. There is a possibility that the permeability value can fluctuate in the first several time steps before it stabilize.

For this micromodel, we have found that the absolute permeability is 0.11285 D. In the following subsections, we will use this micromodel structure for our two-phase flow LBM simulations.

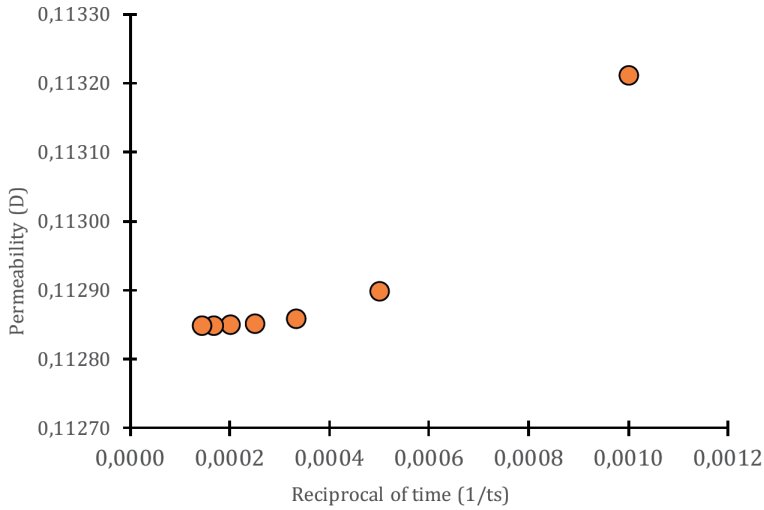

Figure 5.3: Permeability measurement of the micromodel. The permeability measurement initially start with a higher value, then converged to a value as the reciprocal of time goes to zero.

Table 5.1: Fluid properties of the base case (CASE02)

CASEID	CASE02	
Oil Kinematic Viscosity, ν_A	10.7	mm^2/s
Oil specific gravity, SG_A	0.8539	
Water kinematic viscosity, ν_B	1.004	mm^2/s
Water specific gravity SG_B	1	

5.2.2 Base case

The initial case was made as a reference to compare between cases with different fluid properties. The base case has fluids with properties as shown in Table 5.1.

Snapshots of the base case simulation results at four different time steps are shown in Figure 5.4. The pore structure is initially fully saturated with water, and then oil is injected from the left-side (primary drainage process). The red fluid is oil (fluid-A) and the blue fluid is water (fluid-B). The white color represents the grain.

In the figures, we can see that both the displacement mechanism in drainage are captured. The main displacement mechanism is the continuous pore invasion. This is caused by the increase in capillary pressure due to increase in the pressure at the inlet. The other displacement mechanism captured is the *snap-off*, as shown inside the green circles in the

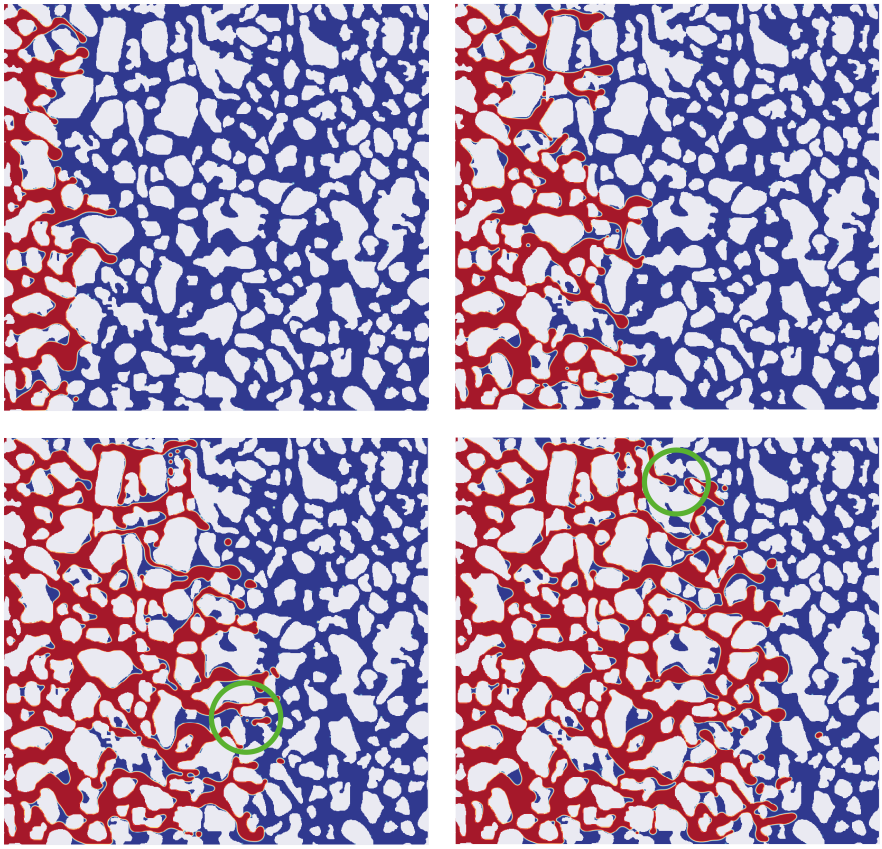

Figure 5.4: Colormap of 'phase' for CASE02 (base case) at **top left**: 100,000 ts, **top right**: 200,000 ts, **bottom left**: 300,000 ts, and **bottom right**: 400,000 ts. The green circles show the location of the snap-off.

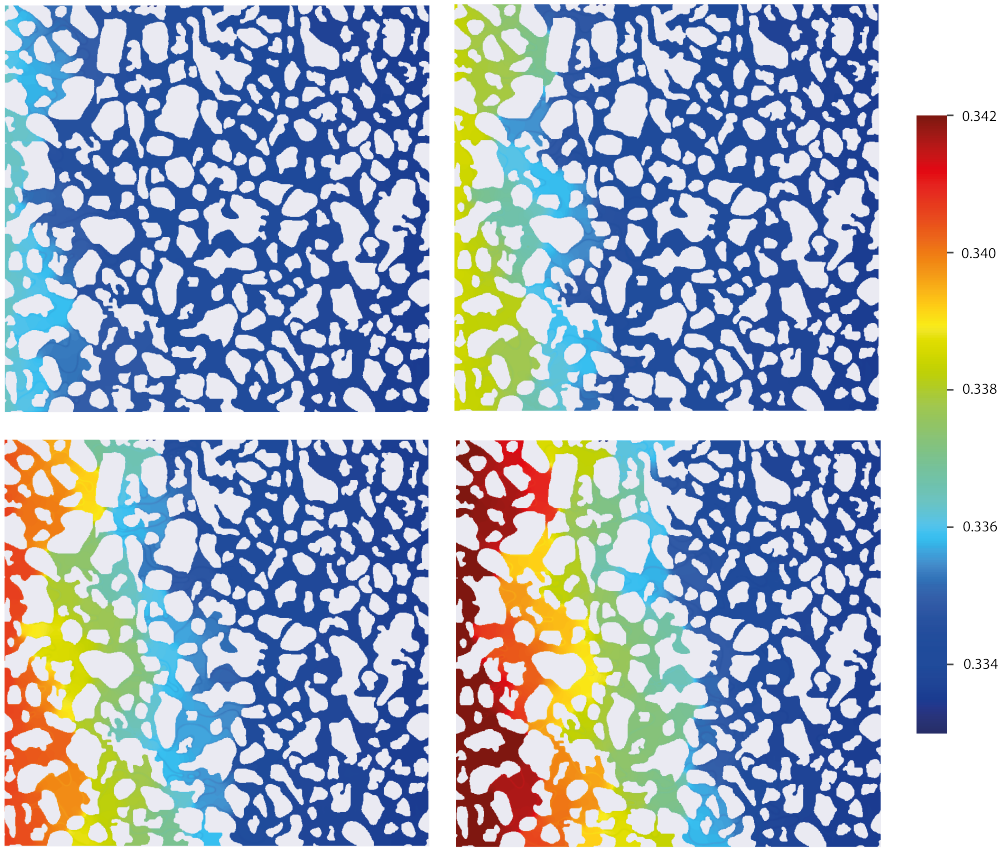

Figure 5.5: Colormap of 'Pressure' for CASE02 (base case) at **top left**: 100,000 ts, **top right**: 200,000 ts, **bottom left**: 300,000 ts, and **bottom right**: 400,000 ts. We can clearly see the increase in pressure as the oil is introduced into the system over simulation time. There is a tiny jump between the two fluid interface, but it is insignifcant compared to the pressure change in the overall micromodel.

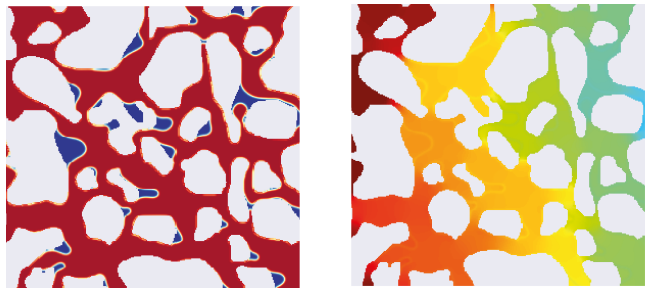

Figure 5.6: Part of the micromodel from CASE02. **Left**: 'phase' color map (fluid distribution) and **Right**: pressure heatmap. Notice that at the fluid interface we can see a tiny pressure jump.

figures. This is due to the capillary forces.

Heatmaps of pressure are shown in Figure 5.5. The pressure at the inlet increase as more fluid-A is injected. Notice that at the interface between the fluids, there is a tiny jump in the pressure (see Figure 5.6), representing the capillary pressure . This shows that the flow is dominated by the viscous forces, instead of the capillary forces. The profile of the pressure in $x-$direction is presented in Figure 5.7. The pressure is calculated by taking the average of pressure in $y-$direction (while ignoring the grain part). The profile clearly shows two different pressure gradients, one for the oil zone and one for the water zone. We define the intersection between the two gradients as the *effective interface* between the oil and water. The effective interface is a location in the micromodel that represent the overall terminal menisci of the invading fluid.

The pressure plot appears to be 'noisy', this is because of the effect of the pore geometry and fluid distribution. The effect of pore geomety is as follows: at the same location x in the micromodel, we can have a significant difference in pressure due to the varying pore sizes (e.g. pore throat vs. pore body) at different y. As a result, the average value in $y-$direction can fluctuate over the micromodel. Similarly, the fluid distribution can also produce the same effect. The oil and water pressure are different and thus the total pressure vary with different fluid distribution. The former factor plays a bigger role since we do not see large effects of the capillary pressure.

To support this reasoning, one can see the similarity in pressure trend locally, where the value between each time step is correlated by some scalar. What is consistent along the micromodel at different time steps is the pore geometry. In fact, the local trend is also observed similarly between different cases that that have different fluid parameters.

In the same plot, the average water saturation is also included (from here onwards, this type of plot is called pressure-saturation plot). We note that the change in pressure gradient corresponds with the change in saturation. The saturation plot do not show a smooth transition along the micromodel, the plot has considerable fluctuation. There are two reasons behind this: snap off and viscous fingering. Snap off causes the water saturation after the effective interface could be less than 100 % (there is a bubble of oil after the effective interface). Meanwhile, viscous fingering creates unstable displacement, hence the

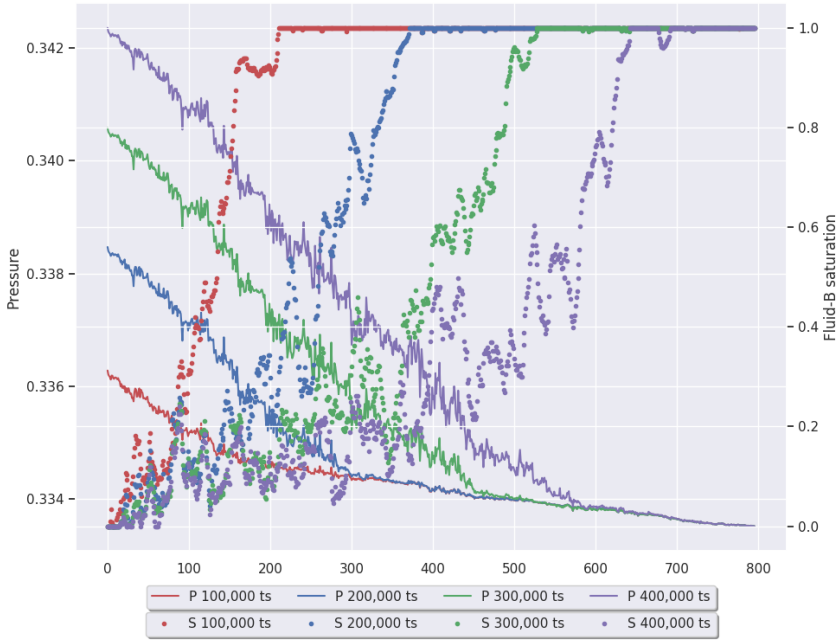

Figure 5.7: Plot of averaged y-direction pressure and saturation for base case.

saturation transition will occur for a longer stretch along the micromodel.

In the following subsections, other simulation cases with different fluid and rock properties were run. These cases are summarized in Table 5.2, where the properties are expressed in lattice unit.

5.2.3 Wettability alteration

First, we considered cases where the wettability was altered. We observed two cases: component affinity of 0 and 0.5, identified by CASE09 (intermediate-wet case) and CASE10 (oil-wet case), respectively. Again, the latter case simulates a imbibition process, because the process is defined by the wettability of the micromodel. Figure 5.8 and Figure 5.9 show the simulation result for these two cases at different time steps. From these figures, there is no significant difference observed in terms of fluid distribution, except for a slight difference in contact angles (see Figure 5.10). One possible explanation for this observation is that in all cases, the flow regime is in the viscous domain, i.e. the flow is dominated by viscous forces with high viscosity ratio. This is supported by the phase diagrams for drainage (Figure 2.4) and imbibition (Figure 2.6).

From the figures, one can also notice that there are oil bubbles accumulated after the front. This is believed to be a numerical error due to initialization of small amount of oil

Table 5.2: Parameters for each case used in the simulation, expressed in lattice unit. The cases are divided into several parts, according to the change in one LBM parameter: **BC**: base case, **VC**: viscosity case, **FC**: flux case, **IC**: interfacial tension case, **WC**: wettability case.

Case ID	CASE01	CASE02	CASE03	CASE04	CASE05	CASE06
$\tau_{A,lb}$	0.58580	0.82100	3.15800	9.71000	0.82100	0.82100
$\tau_{B,lb}$	0.53012	0.53012	0.53012	0.53012	0.53012	0.53012
$\rho_{A,lb}$	0.8330	0.8539	0.9840	0.8270	0.8539	0.8539
$\rho_{B,lb}$	1.0000	1.0000	1.0000	1.0000	1.0000	1.0000
Q_{lb}	5	5	5	5	2.5	10
α	1.00E-04	1.00E-04	1.00E-04	1.00E-04	1.00E-04	1.00E-04
β	0.95	0.95	0.95	0.95	0.95	0.95
Affinity	-0.9	-0.9	-0.9	-0.9	-0.9	-0.9
Ca	1.96E-04	1.96E-04	1.96E-04	1.96E-04	9.80E-05	3.92E-04
M	2.3729	9.1003	86.8351	252.8775	9.1003	9.1003
Remarks	VC	BC	VC	VC	FC	FC
Case ID	CASE07	CASE08	CASE09	CASE10	CASE11	CASE12
$\tau_{A,lb}$	0.82100	0.82100	0.82100	0.82100	0.58580	3.15800
$\tau_{B,lb}$	0.53012	0.53012	0.53012	0.53012	0.53012	0.53012
$\rho_{A,lb}$	0.8539	0.8539	0.8539	0.8539	0.8330	0.9840
$\rho_{B,lb}$	1.0000	1.0000	1.0000	1.0000	1.0000	1.0000
Q_{lb}	5	5	5	5	5	5
α	1.00E-06	1.00E-02	1.00E-04	1.00E-04	1.00E-04	1.00E-04
β	0.95	0.95	0.95	0.95	0.95	0.95
Affinity	-0.9	-0.9	0	0.5	0.5	0.5
Ca	1.96E-02	1.96E-06	1.96E-04	1.96E-04	1.96E-04	1.96E-04
M	9.1003	9.1003	9.1003	9.1003	2.3729	86.8351
Remarks	IC	IC	WC	WC & VC	WC &VC	WC & VC
Case ID	CASE13	CASE14	CASE15	CASE16		
$\tau_{A,lb}$	0.82100	0.82100	0.82100	0.82100		
$\tau_{B,lb}$	0.53012	0.53012	0.53012	0.53012		
$\rho_{A,lb}$	0.8539	0.8539	0.8539	0.8539		
$\rho_{B,lb}$	1.0000	1.0000	1.0000	1.0000		
Q_{lb}	2.5	10	5	5		
α	1.00E-04	1.00E-04	1.00E-06	1.00E-02		
β	0.95	0.95	0.95	0.95		
Affinity	0.5	0.5	0.5	0.5		
Ca	9.80E-05	3.92E-04	1.96E-02	1.96E-06		
M	9.1003	9.1003	9.1003	9.1003		
Remarks	WC & FC	WC & FC	WC & IC	WC & IC		

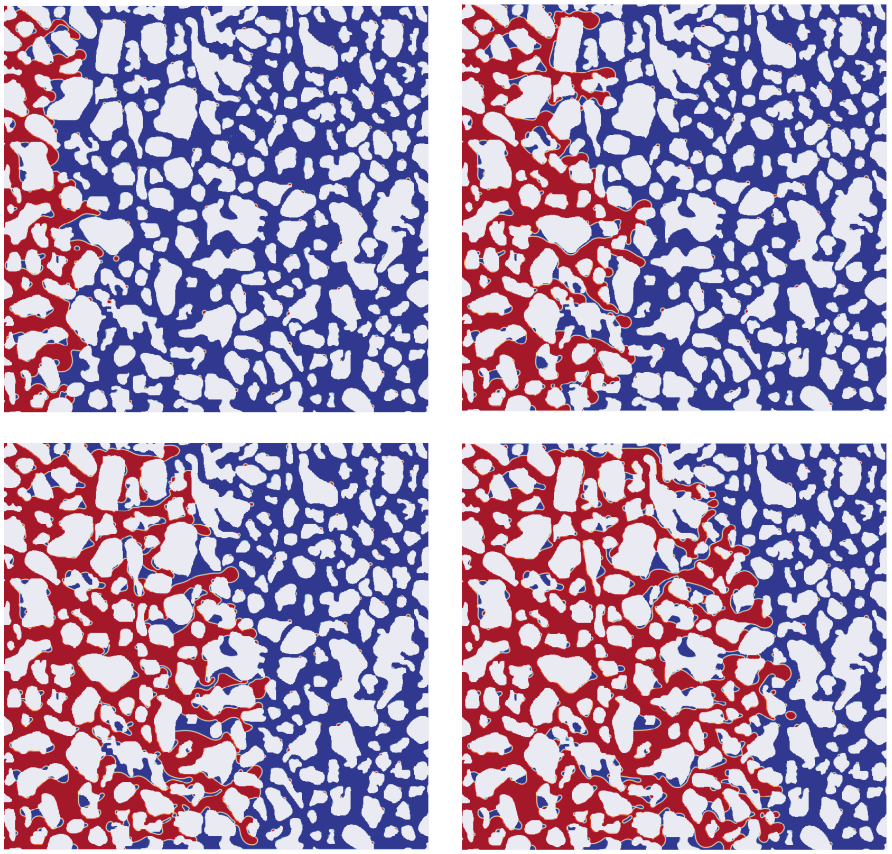

Figure 5.8: Colormap of 'phase' for CASE09 at **top left**: 100,000 ts, **top right**: 200,000 ts, **bottom left**: 300,000 ts, and **bottom right**: 400,000 ts. Small oil bubbles after the effective interface is believed to be a result of numerical error during initialization.

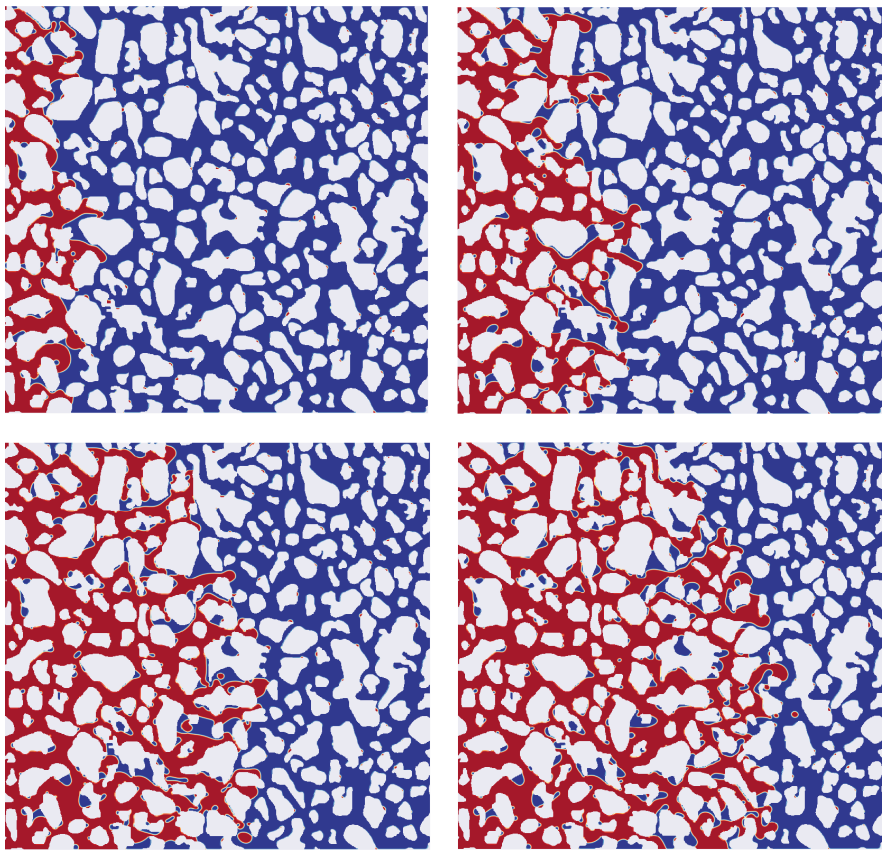

Figure 5.9: Colormap of 'phase' for CASE10 at **top left**: 100,000 ts, **top right**: 200,000 ts, **bottom left**: 300,000 ts, and **bottom right**: 400,000 ts. Similar to CASE09, small oil bubbles after the effective interface is believed to be a result of numerical error during initialization.

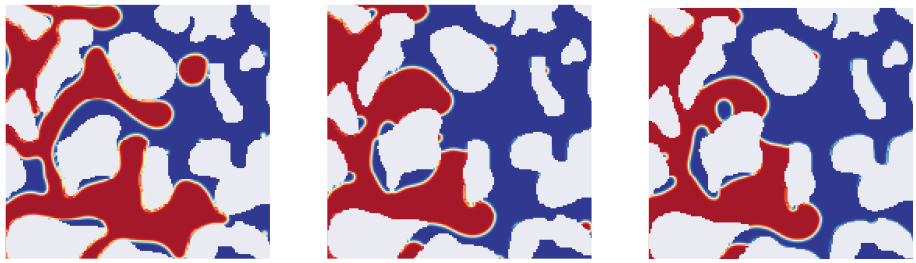

Figure 5.10: Part of the micromodel showing the 'phase' color map (fluid distribution) from **Left**: CASE02 (water-wet), **Middle**: CASE09 (intermediate wet), and **Right**: CASE10 (oil-wet). Notice that there is a difference in contact angle at the terminal meniscii.

phase distribution at every lattice point. During the simulation, this small amount of oil accumulate to form small bubbles that eventually resides at the grain surfaces.

In the following subsections, we will study how the change in viscosity, flux, and interfacial tension affect the simulation result. In each study, we will investigate the case where the micromodel is oil wet, by changing the component affinity to 0.5. The result of each study will be discussed in the corresponding subsection.

5.2.4 Change in viscosity

For oil reservoir, we have larger difference in oil (fluid-A) properties rather than water (fluid-B) properties. One of the most important properties that affect the fluid displacement in the reservoir is the oil viscosity. In this subsection, we observe four other simulation results from four different oil viscosity values. The four cases are: CASE01, CASE02 (base case), CASE03, and CASE04. In this case, CASE01 has the lowest oil viscosity and CASE04 has the highest viscosity.

Figure 5.11 shows the fluid distribution of all four cases at the last time step. As seen from the figures, at lower viscosity, oil travels further compared to the higher viscosity at the same pore volume injected, and vice versa. Higher oil viscosity creates a more stable displacement: there is less bypassed water behind the front. Consequently, we will observe a sharper front for higher viscosity (see Figure 5.12). This is in agreement with the phase diagram for the drainage process (see Figure 2.4), where high viscosity ratio results in stable displacement.

This observation is also supported by the pressure-saturation plot, as shown in Figure 5.13, Figure 5.14, and Figure 5.15. From the figures, one can also observe the change of the pressure gradient between cases. The higher the viscosity, the larger the pressure gradient. This is consistent with what we would expect: that to have equal flux rate, one needs higher pressure at the inlet boundary for a more viscous fluid.

According to Darcy's law, pressure drop and dynamic viscosity are proportional to each other. Based on the pressure plot, we divide the two phase regime: before and after the effective interface. We calculate the pressure gradient for both regimes. The ratio of the pressure gradient is expected to be similar to the ratio of the dynamic viscosities of the two fluids, since the pore structure is relatively homogeneous:

$$\frac{\nabla P_A}{\nabla P_B} = \frac{q\mu_A/k}{q\mu_B/k} = \frac{\mu_A}{\mu_B} \tag{5.2}$$

Figure 5.16 shows the plot corresponding to Equation 5.2 for the viscosity change cases. The simulation results are represented by the green line, and the theoretical relationship is represented by the dashed orange line. Here, we see that the simulation results show good agreement compared to the theoretical line. One possible explanation for the deviation is

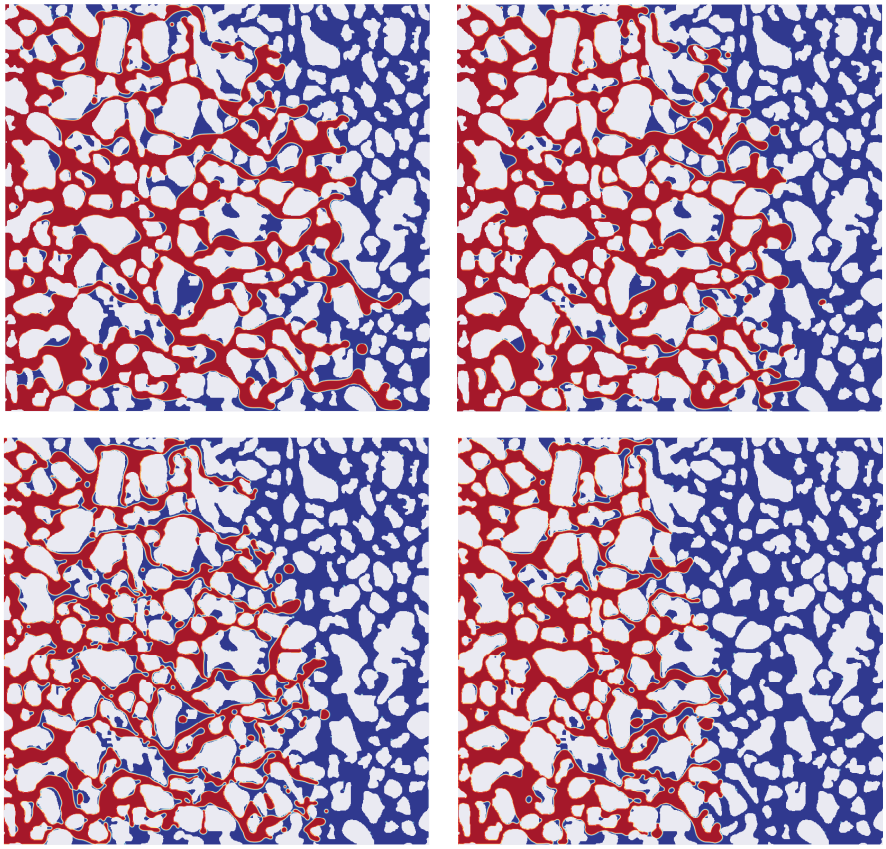

Figure 5.11: Colormap of 'phase' at time step 400,000 ts for **top left**: CASE01, **top right**: CASE02, **bottom left**: CASE03, and **bottom right**: CASE04. For CASE03, fluid distribution due to 'pivot' effect is seen clearly at the last time step.

Figure 5.12: Averaged $y-$direction water saturation plot of CASE01, CASE02, CASE03, and CASE04. Lower viscosity oil advances further into the micromodel.

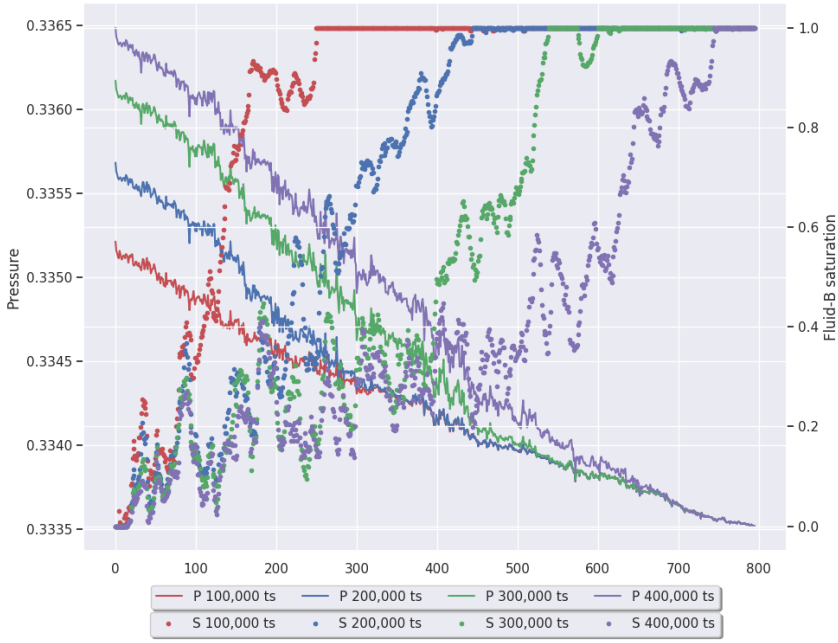

Figure 5.13: Plot of averaged y-direction pressure and saturation for CASE01.

that the saturation behind the front is not completely filled with fluid-A, hence representing relative permeability. Other possible explanation is due to difference in permeability before and after the effective interface. Another interesting observation is the difference in fluid distribution for medium-high-viscosity CASE03 compared to the other cases (see Figure 5.11). We will address this issue in the subsection 5.2.7.

Next, we would like to see the effect of the change in viscosity in an imbibition process. Here, we have the component affinity of 0.5, with increasing viscosity in CASE11, CASE10, and CASE12, respectively. The simulation results are shown in Figure 5.17. Similar to drainage prcess, we also observe that with lower viscosity oil is moving further into the micromodel. The simulation with higher oil viscosity is able to displace water behind the front more efficiently, and therefore resulting in a more stable displacement. This is as expected, based from the phase diagram for imbibition.

Similar to the previous subsection, we do not observe any significant difference in fluid distribution, except for slight difference in contact angle.

5.2.5 Change in flux

Operational condition such as injection rate can affect the fluid distribution. In this part, we observe the fluid distribution at three different injection rate (Q_{lb}): 2.5, 5.0, and 10.0.

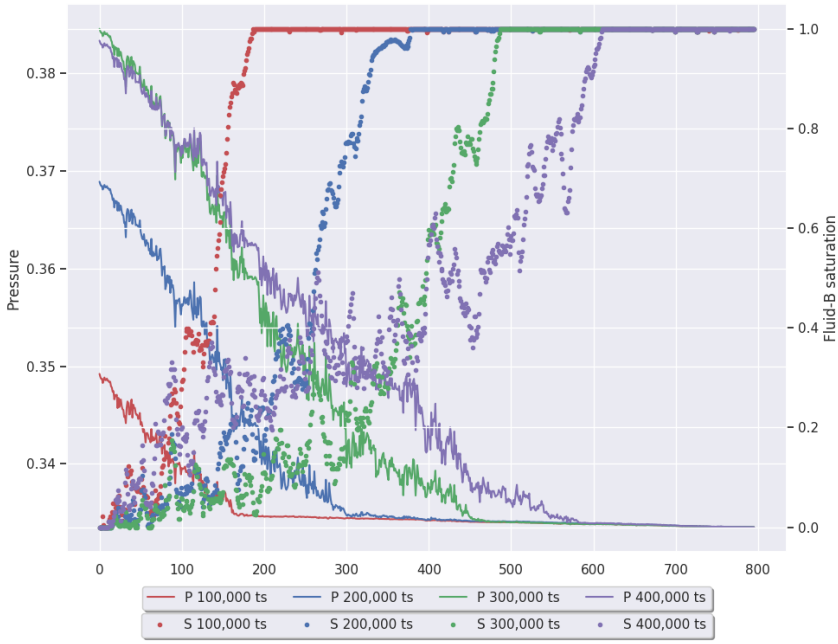

Figure 5.14: Plot of averaged y-direction pressure and saturation for CASE03. Notice a drop in inlet pressure at the last time steps, followed by an increase in water saturation behind the effective interface. This is caused by the 'pivot' effect.

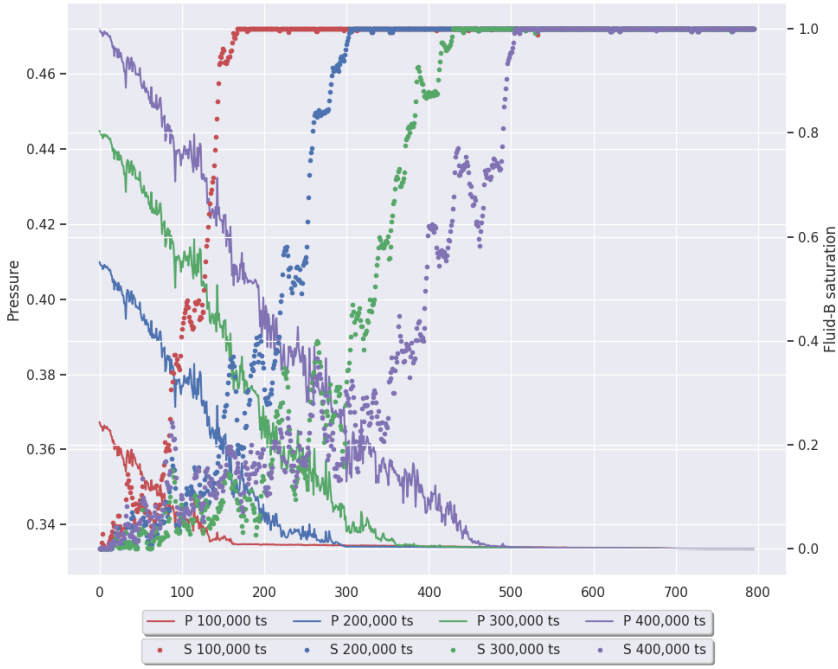

Figure 5.15: Plot of averaged y-direction pressure and saturation for CASE04.

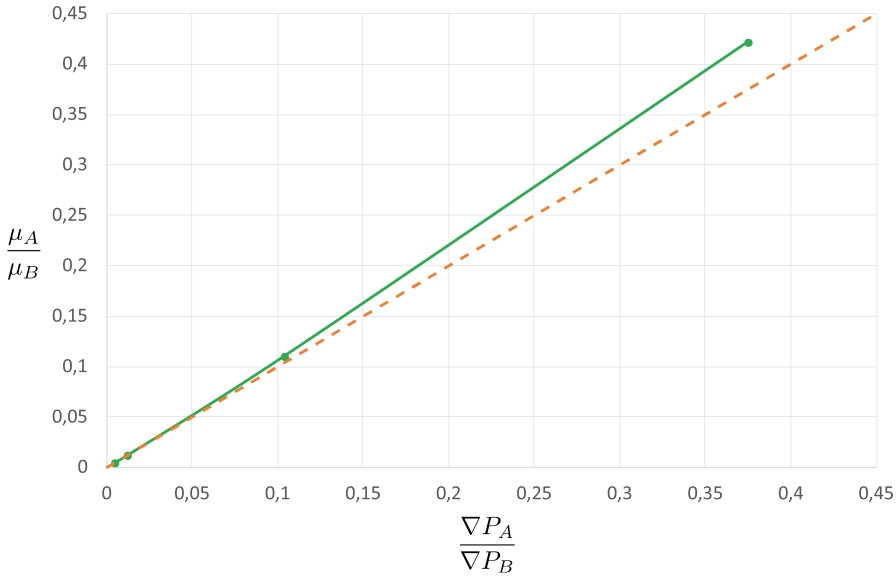

Figure 5.16: Plot of pressure drop ratio vs dynamic viscosity ratio. P_A and P_B are the total pressure behind and after the effective interface, respectively. μ_A and μ_B are the fluid-A and fluid-B viscosity, respectively. The green dots are the data points from the simulation, while the dashed orange line is the theoretical calculation.

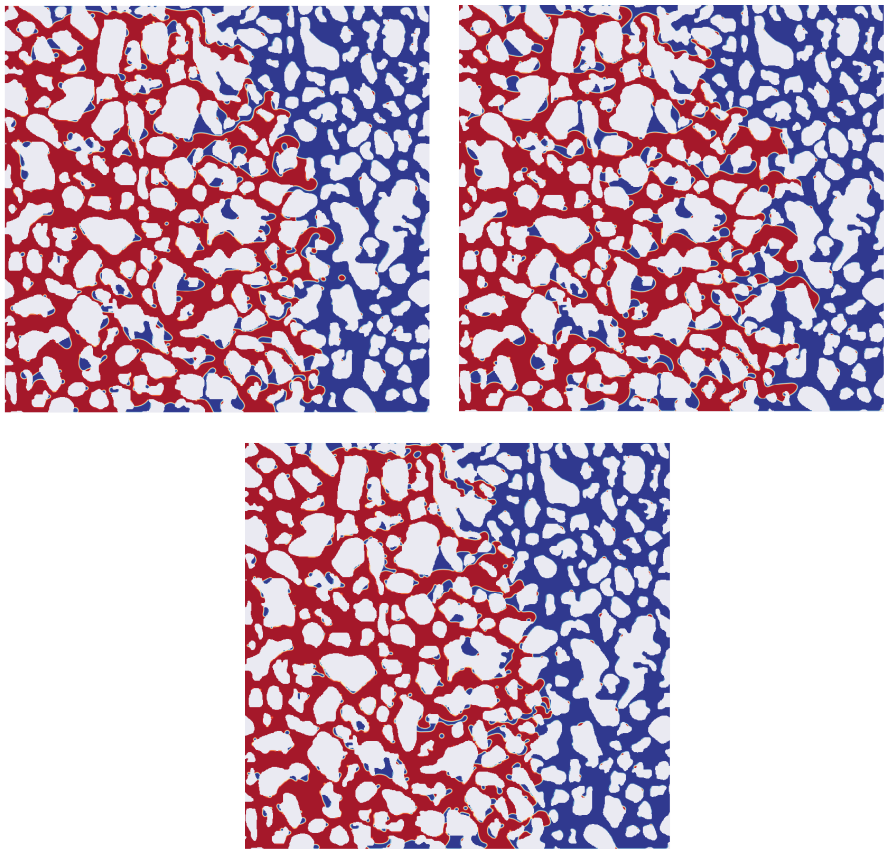

Figure 5.17: Colormap of 'phase' at time step 400,000 ts for **top left**: CASE10, **top right**: CASE11, and **bottom**: CASE12.

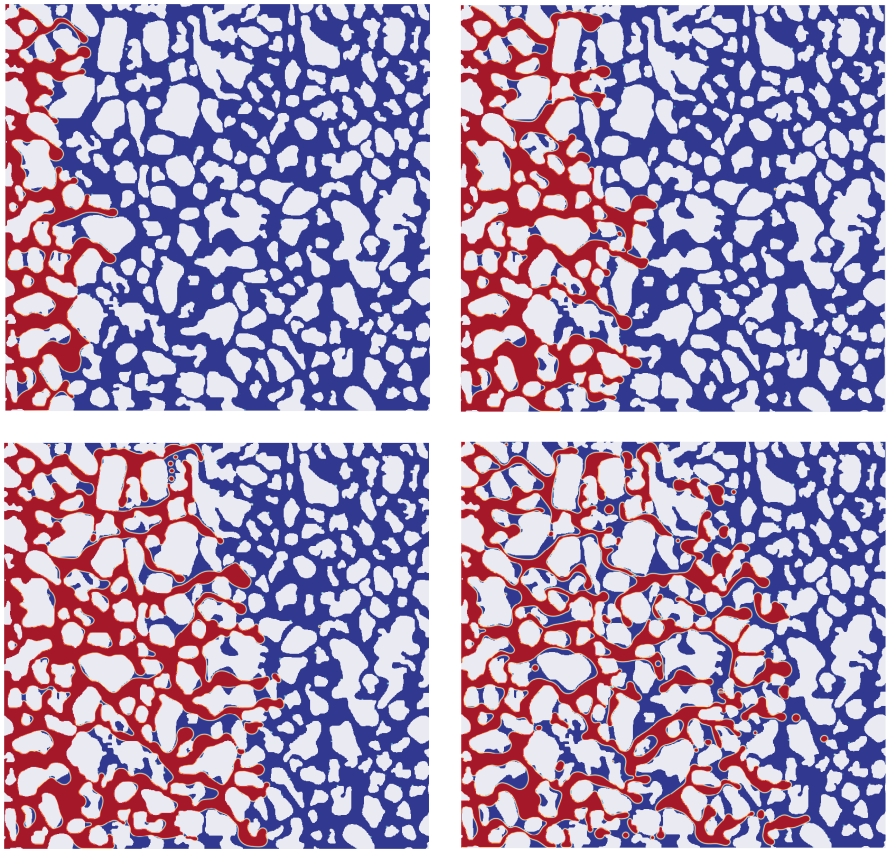

Figure 5.18: Colormap of 'phase' for CASE05 at **top left**: 200,000 ts (500.000 TVI), **top right**: 400,000 ts (1.000.000 TVI), **bottom left**: 600,000 ts (1.500.000 TVI), and **bottom right**: 800,000 ts (2.000.000 TVI). Fluid distribution due to 'pivot' effect is seen clearly at the last time step.

The corresponding case identifiers are (in the order of increasing injection rate): CASE05, CASE02, and CASE06. CASE05 has an injection rate half of CASE02, and CASE06 has an injection rate double of CASE02. Figure 5.18 and Figure 5.19 show simulation results at 4 different time steps. Notice that the time step is chosen such that the total volume injected is the same for each case. The total volume injected is calculated by:

$$TVI = Q_{lb} \times t \tag{5.3}$$

where TVI is the total volume injected, Q_{lb} is the flux, and t is the simulation time. The four TVIs compared in this thesis are: 500.000, 1.000.000, 1.500.000, and 2.000.000.

From the figure, there is no significant difference in fluid distribution between medium-

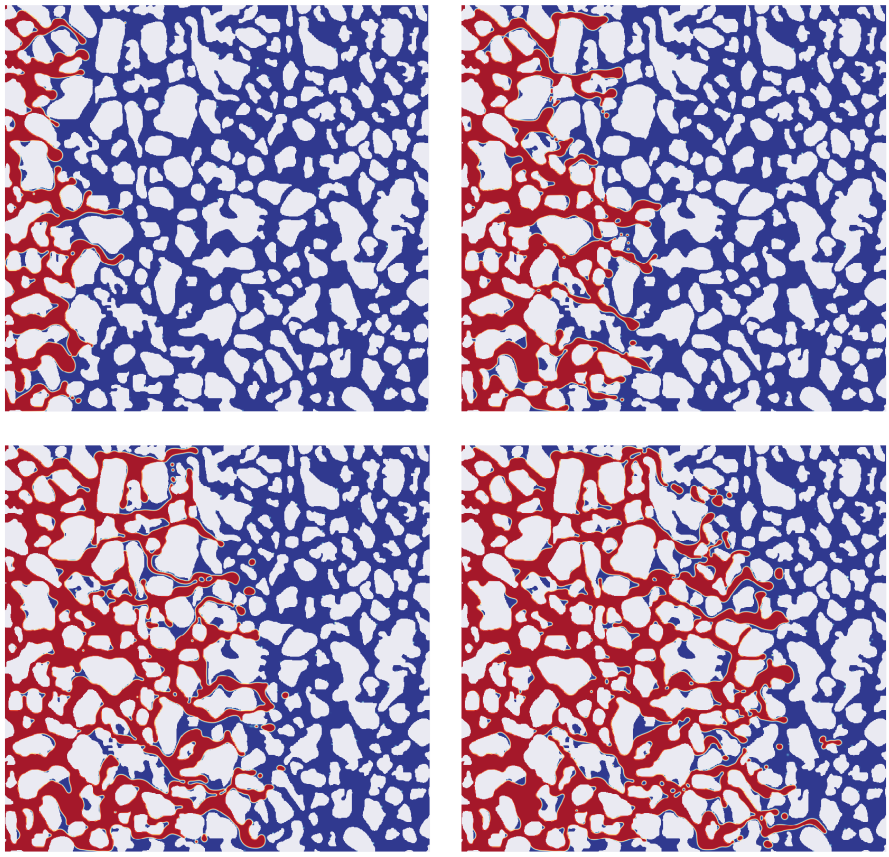

Figure 5.19: Colormap of 'phase' for CASE06 at **top left**: 50,000 ts (500.000 TVI), **top right**: 100,000 ts (1.000.000 TVI), **bottom left**: 150,000 ts (1.500.000 TVI), and **bottom right**: 200,000 ts (2.000.000 TVI).

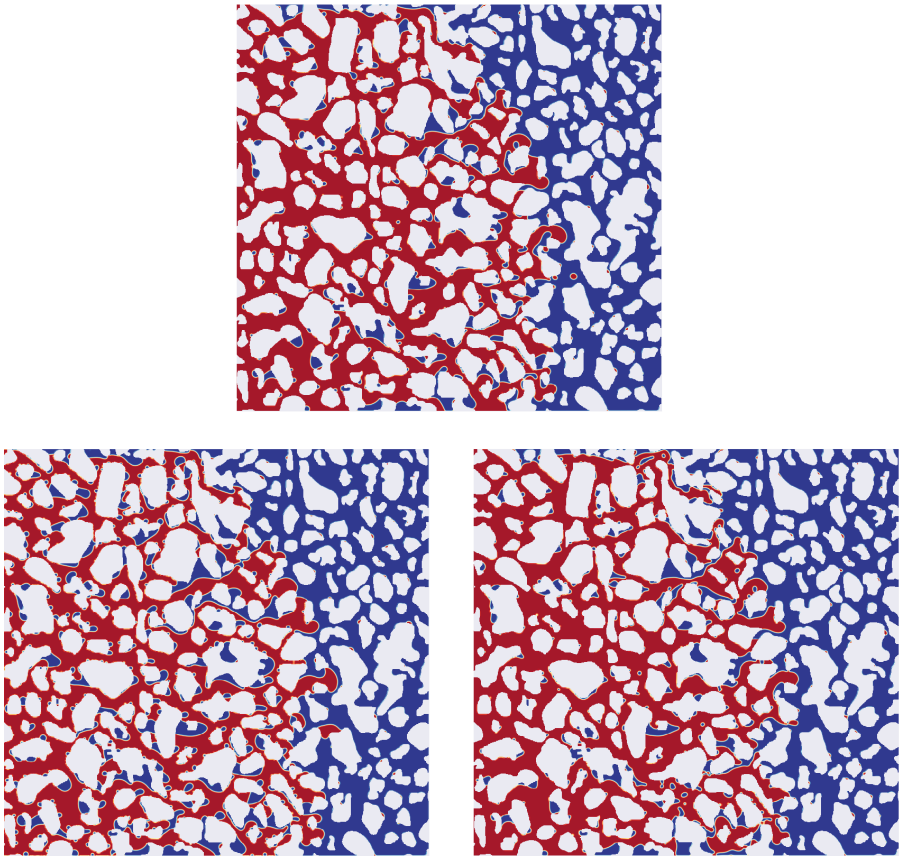

Figure 5.20: Colormap of 'phase' at 2.000.000 TVI for **top**: CASE10, **bottom left**: CASE13, and **bottom right**: CASE14.

flux CASE02 and high-flux CASE06 for all investigated TVI values. We can only see a slightly more effective displacement in medium-flux CASE02. This is expected, based on the phase diagram (see Figure 2.4), where higher capillary number (lower velocity) corresponds to a more stable displacement. Now, we observe what happens when the wettability is set to 0.5. Three cases are observed: CASE13, CASE10, and CASE14. The corresponding injection rates are: 2.5, 5.0, and 10.0, respectively (expressed in lattice unit). Figure 5.20 shows the fluid distribution at 2.000.000 TVI for all the three cases.

From the figures, we see no significant difference in CASE10 and CASE14 in terms of fluid distribution. However, in the low-flux CASE13 we see a lot of water bubbles formed before the front. In addition, the oil advanced slightly further compared to the other cases, and there is more water volume before the front. This shows that high-flux CASE13 has a less stable displacement compared to the other two cases (arguably, medium-flux CASE10 also has a less stable displacement as compared to CASE14 based on the fluid distribution). This as expected based on Figure 2.6, where higher capillary number (higher flux) leads

to a more viscous dominated displacement.

5.2.6 Change in interfacial tension

In this part, the effect of interfacial tension between the fluids to the fluid distribution is observed. We have found out that if the 'alpha' in Equation 3.9 (denoted by A in the equation) cannot be too low. Low-interfacial-tension cases such as CASE08 and CASE16 run into numerical error and therefore will not be analysed in this subsection. The likely cause to this is that during the optimization routine (Equation 3.11), the low value can initiate numerical instability to the solver.

Here, we compare CASE02, CASE07, CASE10, and CASE15. The first two has the wettability of -0.9, and the last two has the wettability of 0.5. Also, CASE07 and CASE15 has interfacial tension of 100 times greater than the other two. The result of the simulations are shown in Figure 5.21 at 400.000 ts.

From the figure, we see that the fluid distribution is similar for cases with the same wettability. However, there is only a slight difference between the wettability of -0.9 to 0.5. The most notable difference is that for the wettability of -0.9, the terminal menisci has a clear drainage-like menisci displacement. For the simulation with the wettability of 0.5, some of the oil at the front sticks to the solid surfaces.

Difference in 'alpha' value does not give clear distinction in fluid distribution. This becomes more apparent by observing the partial pressure of all four cases. The plots are shown in Figure 5.22. We would expect to have a higher gap between oil and water pressure values (to represent capillary pressure), but when 'alpha' is increased, there is no considerable difference in capillary pressure between the two cases. Further, we see a lower pressure at the inlet when the 'alpha' value is higher. This contradicts the fact that the defending fluid should be easier to be displaced by the incoming fluid with lower interfacial tension between them.

This raises a question whether we are unable to model the intended realistic process. With given injection rate and pore structure, the effect of the viscous force is too large compared to the capillary forces in the simulation. To solve this problem, one can try either by decreasing the flux or fluid viscosity. In this study, we have tried to decrease the fluid viscosity. Decreasing it even further leads to unstable numerical simulation. The issue with decreasing the flux even further is that the computational cost is too much.

5.2.7 Abnormalities

So far, we have simulated several two-phase flow cases by changing one parameter at a time. Interestingly, abnormalities occur in few of these cases. Some of them are minor abnormalities, e.g. small oil bubbles in front of the effective interface, local pressure fluctuations, and numerical instabilites when the 'alpha' value is too low. These abnormalities can be explained with great certainty. However, there are thee major issues that has to

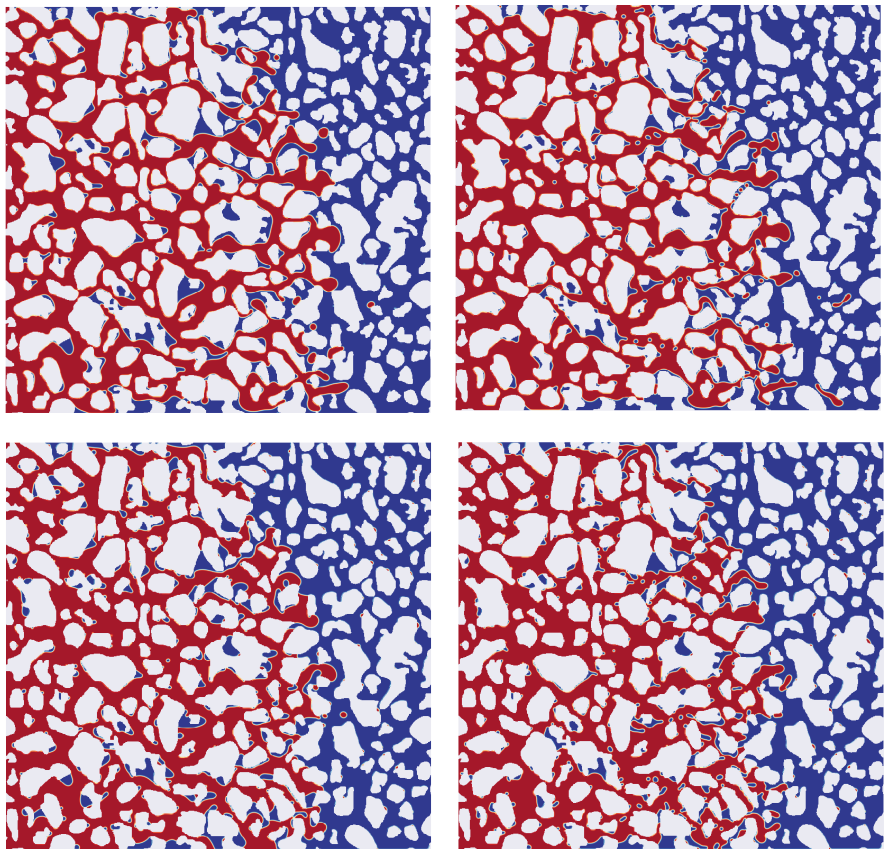

Figure 5.21: Colormap of 'phase' at 400.000 ts for **top left**: CASE02, **top right**: CASE07, **bottom left**: CASE10, and **bottom right**: CASE15.

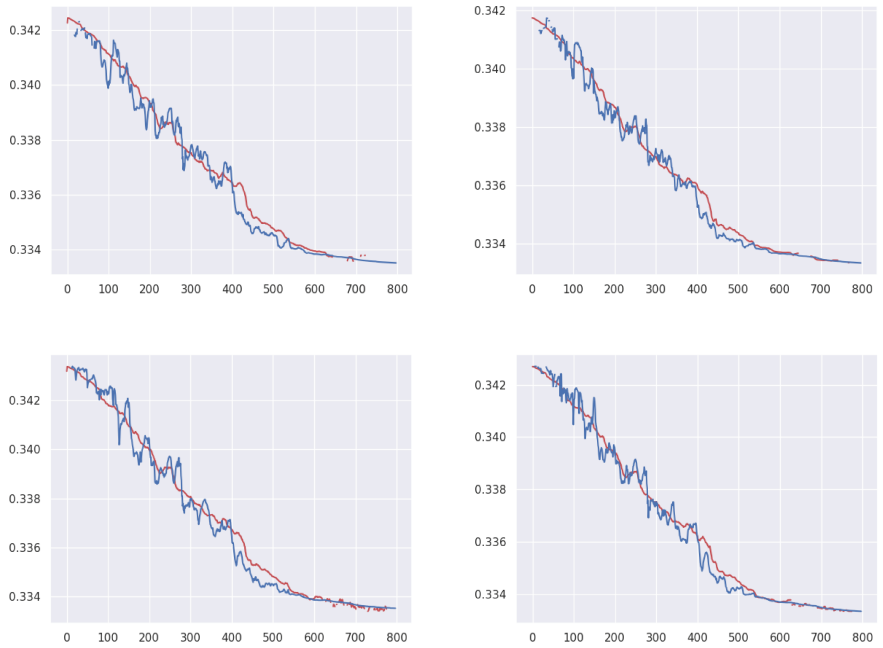

Figure 5.22: Oil pressure (red) and water pressure (blue) at 400.000 ts for **top left**: CASE02, **top right**: CASE07, **bottom left**: CASE10, and **bottom right**: CASE15.

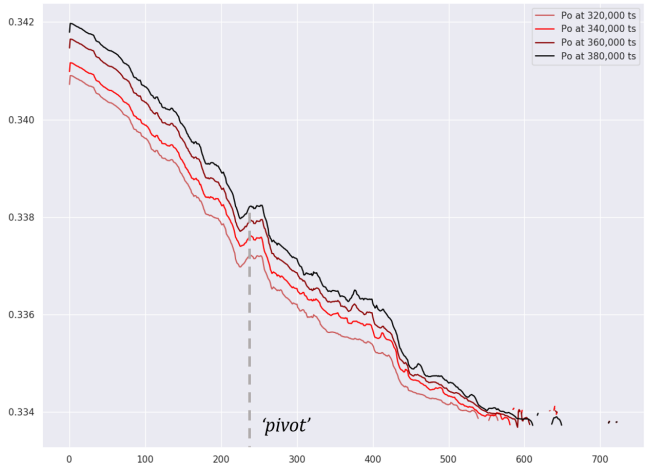

Figure 5.23: Average partial oil pressure (P_o) for CASE02. 'Pivot' location is denoted by the grey dashed line.

be addressed in this study: the pivot effect, the lack of capillary pressure effect, and the improper imbibition process.

The pivot effect

The most notable one is the abnormalities of the fluid distribution in medium-high-viscosity CASE03. If we look at the average pressure plot (Figure 5.14), we see that the pressure at the inlet drops at 400,000 ts. In the same plot, the saturation plot also shows that the water saturation increase behind the effective interface at late time steps. The plot suggests that the oil saturation is smeared out, without change in volume. To investigate the problem, partial pressure for both phases are plotted at time steps around when the pressure at the inlet starts to drop. We suspect that the water partial pressure after the front is higher than the water before the front, therefore the total pressure before the front relaxes. This can only occur if the water before and after the front is connected. To compare, we also show the same plot for base-case CASE02. The plots for CASE02 are shown in Figure 5.23 and Figure 5.24. The plots for CASE03 are shown in Figure 5.25 and Figure 5.26.

In both cases, the partial pressure follows the trend of the total pressure. For CASE02, the pressure keeps increasing as the time step increases. This is not the case for CASE03. We see that the problem starts at the time steps between 340,000 ts and 360,000 ts. For both cases, we see there is a slight jump in pressure at around 230 voxels from the left side of the micromodel. This is also the location in which the pressure becomes the 'pivot' for CASE03: the pressure after this pivot increases and the pressure before this pivot decreases

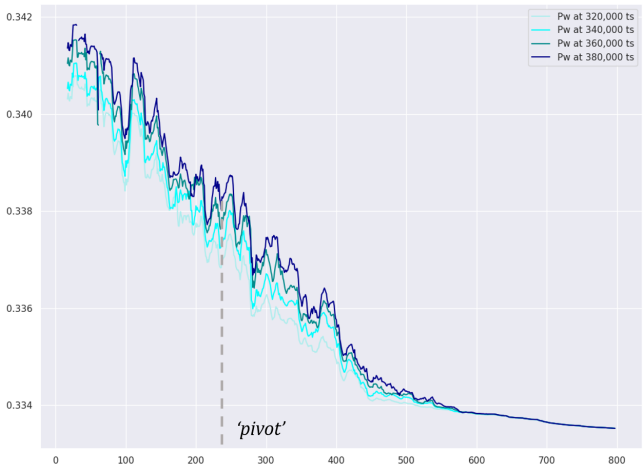

Figure 5.24: Average partial water pressure (P_w) for CASE02. 'Pivot' location is denoted by the grey dashed line.

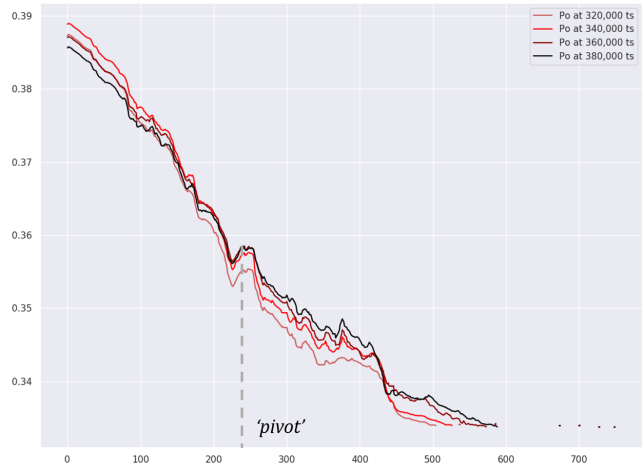

Figure 5.25: Average partial oil pressure (P_o) for CASE03. 'Pivot' location is denoted by the grey dashed line.

Figure 5.26: Average partial water pressure (P_w) for CASE03. 'Pivot' location is denoted by the grey dashed line.

over time. It seems like the 'pivot' limits the pressure propagation. Note that for CASE03 in Figure 5.26, the water pressure before this 'pivot' location stabilizes: the water pressure has less fluctuation. This proves that the water is connected before and after this 'pivot' location. This is also shown in the 'phase' colormap where fluid pinch-off happens more often before this point. After this location, the water pressure increases. On the contrary, CASE02 has a constant increase in water pressure for all time steps.

We can see the similar behaviour in CASE05 at 2.000.000 TVI. Here, pinch-off occurs rapidly before the front. At this point, we see that the water becomes connected before and after the fluid front. This is the same behavior as the one observed in CASE03. Figure 5.27 and Figure 5.28 show the partial pressure for oil and water, respectively, around the time when the problem occurs. Similar to the problem that occurs in CASE03, the water pressure stabilizes before the 'pivot' location.

The reason why CASE03 and CASE05 are the only cases where this problem occurs remain a mystery. Perhaps, the combination of the fluid properties, injection rate, and pore geometry allows the 'pivot' effect to happen. Of course, there is also a possibility that there is something wrong with the implementation boundary condition in LBPM. However, this is not likely to be the case since the other cases should encounter the same problem.

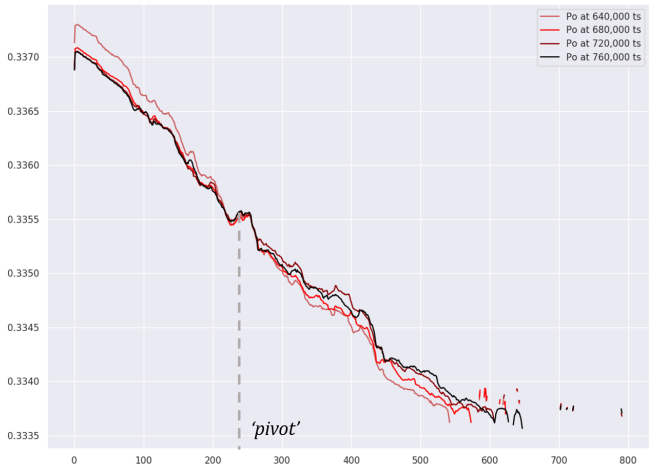

Figure 5.27: Average partial oil pressure (P_o) for CASE05. 'Pivot' location is denoted by the grey dashed line.

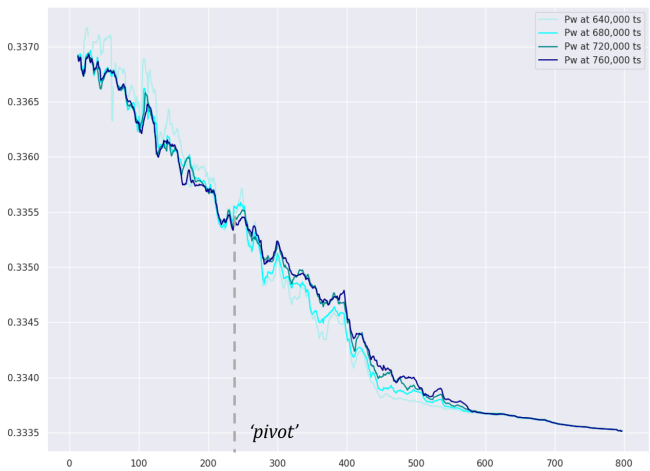

Figure 5.28: Average partial water pressure (P_w) for CASE05. 'Pivot' location is denoted by the grey dashed line.

Lack of capillary pressure effect

One of the major issue in this study is that there seems to be no significant effect of capillary pressure in the simulation. This is particularly shown in subsection 5.2.6, where the capillary pressure still does not give any effect even if the interfacial tension is increased by two orders of magnitude. In addition, all other cases are dominated by viscous force, with little to no capillary pressure effect (shown in every pressure plot and pressure heatmaps). As previously discussed, this can be resolved by having a lower viscosity fluid or to reduce the flux considerably. Another possibility is to improve the resolution of the model (in time and space). This however, comes with high computational cost, especially because in LBM, space and time grid refinement go hand in hand. Ideally, we can resolve this problem using better hardware e.g., more CPU use or a GPU implementation. Whether implementing this solution to the problem is feasible or not depends on the research objective and available resource.

We see also that when the 'alpha' is set too low (CASE08 and CASE16) we encounter numerical issues. This tells us that there is a lower limit to the 'alpha' values that can be considered. This can limit the applicability of LBM. To overcome this problem, one can try to formulate another solver to the optimization problem in order to solve the redistribution of particles in the color gradient method.

Improper imbibition process

During the drainage process, we have observed pore invasion and snap-off, as described in the previous chapter. We see that the simulation result is in agreement with the phase diagram for the drainage process. However, during the imbibition process, pinch-off and piston-like throat filling do not occur as described in chapter 2. As a consequence, the fluid distributions do not appear as expected in the phase diagram for the imbibition process. Arguably, it is unrealistic to expect the theoretical fluid distribution in the imbibition process as in Figure 2.6, since it is derived from a very simple network model. Still, one might be able to observe the desired fluid distribution in an even more oil-wet solid. Further, from the droplet case we know that the contact angle does not necessarily have a linear correlation with the component affinity, specifically when the component affinity is greater than 0. This can affect the local fluid displacement, and the overall fluid distribution in the micromodel.

Another possible explanation is that because the flow is so viscous dominated, it has a velocity profile similar to single-phase flow. In single-phase flow, the velocity near the solid is reduced and the velocity near the middle of the pore is the highest. If this effect on the oil phase (since oil is injected) is significant, we will see a change in contact angle.

Chapter 6

Conclusion

In this thesis, we have reviewed the fluid displacement in porous media. We started with the fundamental interaction between the fluids and solids, then applied this knowledge to explain the two-phase flow in a porous media. As a result, we were able to explain some displacement in two main displacement processes in the reservoir: drainage and imbibition.

We have reviewed the basics of LBM, e.g. the general equation, the boundary conditions, and its limitation. LBM is a convenient fluid flow method for simulation directly at digital pore image, due to its simple implementation. The method is extended to two-phase by using colour gradient method. We use dimensional analysis to convert from physical unit to lattice unit.

We have conducted two-phase LBM simulations using LBPM software. Several cases have been set up and run according to parameters of interest. The simulation results are processed, visualized, and analyzed to get a more understanding of the model. Several key points that can be inferred from the simulation are:

- We have confirmed that the component affinity is linearly correlated with the contact angle. This also tells us that the component affinity is dependent on the interfacial tension between the fluid and the solid, scaled by the interfacial tension between the two fluids.
- We have measured the absolute permeability of the pore structure by simulating a single-phase flow using LBM. The measured permeability starts at a higher value and then stabilized to a converged value due to the bounce-back boundary effect at the solid. The result is converged to 0.11285 D
- We have found that we can reproduce some known displacement mechanisms, mainly the pore invasion and snap-off during the drainage process. The displacement mechanism for imbibition processes do not appear as clearly.

- When the viscosity is changed, we can observe the change in pressure drop in the oil phase that corresponds to the change in viscosity. This is confirmed by Figure 5.16. Further, different fluid distributions are observed at different viscosities, and are in agreement with phase diagrams from the literature.
- In the flux change cases, we have found that with equal TVI, the effecitve interface advances around the same location for different flux. There is a major issue with the pressure drop at the inlet for low-flux CASE05, and this is due to the 'pivot' effect. The 'pivot' effect occurs when the location of the 'pivot' prevent the pressure from propagating further into the model. This is due to a jump in pressure before the 'pivot' location. Here, the water seems to move against the flow and becomes 'connected' throughout the micromodel.
- We do not see any significant difference in fluid distribution when the interfacial tension is increased. We also have not found any difference in the capillary pressure from the partial pressure plot. We have also found that lower interfacial tension have more threshold pressure, which contradicts the basic theory of threshold pressure.

While the above points give us useful information regarding our model, we also found out that it has rooms for improvement. Based on this study, we concluded that LBM is able to simulate two-phase fluid flow in a porous medium, given that the objective of the study is clear. The objective of the study must include the operating condition, physical parameters, and the scale of interest. If all of these requirements are unambiguous, then one can theoretically set the necessary LBM parameter in order to obtain the desired result. The LBM parameters, of course, has to obey the hard constraint from the LBM simulation in order to avoid numerical instability. However, to get to this point, one needs to do trial-and-error, and it may take some time to obtain the correct setup.

Referring back to the main objective of this thesis: is LBM a proper tool to simulate a two-phase flow in a porous media? The answer to this question is not straightforward. As we have seen from the results in the previous subsections, we found both consistency and abnormalities in our simulation results. This shows that even though LBM is able to simulate two-phase flow in porous media, it clearly has some limitations.

Previously, in the 'Specialization Project', we have found that LBM can reproduce classical single-phase fluid flow dynamics: Poiseuille flow and flow around a cylinder. In this study, we have shown that LBM can reproduce some of the typical two-phase flow displacement phenomena in porous media. For example, in the droplet case, we managed to get the desired contact angle by setting the component affinity.

In the micromodel flooding case, we are able to set up the LBM parameters such that it represents the experimental condition. Firstly, we set up the pore structure of the micromodel and its resolution in time and space, Then, we convert every important parameter from physical units to lattice units. From the simulation results, we obtained some of the typical displacement mechanisms: pore invasion and snap-off in the drainage process. However, we do not see such clear displacement mechanism in the imbibition process. We have a clear distinction between the fluid distribution for viscosity and flux change cases, and a slight difference for wettability cases. The resulting fluid distributions are also in

agreement with the phase diagrams, based on its capillary number and viscosity ratio. We do not see any significant difference when changing interfacial tension, due to the flow being dominated by viscous forces.

On the positive side, the domination of the viscous force allows us to confirm several points. First, we have confirmed that the pressure drop along the micromodel is in agreement with the viscosity of both fluids. Here, we have used the term effective interface to divide the two parts of the micromodel, based on the location of the intersection between the two pressure gradients. Second, we are able to confirm that the fluid displacement during the drainage and imbibition process is relatively stable, for a system with high viscosity ratio. On the other hand, when the viscosity ratio is small, we would have a less stable displacement. This is in agreement with the theoretical phase diagram.

We encountered some major abnormalities such as the 'pivot' effect, lack of capillary pressure effect, and improper imbibition process. These abnormalities have a significant impact on the simulation results, and thereby give unexpected fluid-flow behavior. These abnormalities have been discussed and suggestions to improve the simulation has also been presented. This means that not only LBM has to operate inside some restricted range to function successfully, but also that LBM has to be conditioned such that the simulation can produce the desired result. For example, in our study we found out that we can only see the effect of the capillary force if we reduce the injection rate. This, however, might not be possible if the required computational resources are not available.

On another note, we have found that LBPM is a reliable tool to simulate LBM. In most cases, the LBPM is able to give a stable two-phase flow simulation in the micromodel. Most of the parameters set in the LBPM seems to represent the desired properties, both for the fluid part and solid part, except for interfacial tension. LBPM run smoothly with a wide range of fluid parameters, and rarely encounters any instability. We also have successfully implemented parallel computation in this study, which helps speed up the LBM simulation. However, when LBPM is run for many time steps, sometimes the simulation stuck, so one had to restart the simulation from the previously saved time step. The reason behind this issue is still unknown.

The data from the simulation results can be extracted, processed, and visualized as we have shown in this study. As explained in the first chapter, this is one of the essential things to consider to have a more fundamental understanding of what is happening in the model. Here, we have shown that we can use the data to do the necessary analysis in order to solve the specific problem of interest.

Chapter 7

Recommendation

Given time constraints for this thesis, we did not have the opportunity to run an LBM simulation for a much lower injection rate. Lower injection rate allows observations in a capillary dominated region, where it will be interesting to see whether LBM can reproduce assumed behavior. The LBPM software has a capability to run on GPU clusters, which was not implemented in this thesis. Generally, GPU performs calculations much faster than CPU, and therefore is able to handle bigger models (higher resolution image in terms of time and/or space).

We did not have the time to test different pore structures. The pore structure used in the simulation is homogeneous, which allows for a fairly uniform fluid displacement. In a heterogeneous rock, the fluid displacement can occur differently and the effect of pore geometry will be apparent. Further, since the simulation has periodic boundaries and identical pore structure in $z-$direction, the simulation is representing a flow in 2-dimensional space. This allows a clear visualization of simulation result and is able to reproduce basic fluid flow behavior in porous media. However, the microfluidic chip in the experimental setup has a boundary layer on the top and the bottom of the chip. In this case, the fluid curvature is also dependent on the curvature in $z-$direction. To really represent the flow in a micromodel, one needs to consider the boundary layer on the top and the bottom of the model. It would also be interesting to test out different the micromodel size. The considered micromodel might be too small to distinguish fluid distribution between different cases. The effect at a certain location might be affected by the nearby location, where in our case might be the whole micromodel. One can try to simulate LBM in a bigger micromodel in order to remove this effect.

The unsolved questions from this thesis can be divided into two parts. The first part is that we are not able to see the effect of the capillary forces due to viscous forces being too dominant. The solution to this part is to have more computational resources. The resources can be in terms of computational power (GPU implementation) or other resources (more time and/or being more efficient by knowing the correct simulation setup).

The second part is that we encounter the pivot effect and the problem with interfacial tension being inconsistent at the boundary. For the former case, a further study needs to be done to check whether a certain fluid distribution allows such effect to occur. Further, we need to know what is the underlying cause. For the latter case, it is likely to be caused by the incorrect implementation of boundary condition. One can try to develop a new method to compute a more accurate boundary condition.

Lastly, to compare between the experimental result and the simulation result, all of the necessary simulation parameters must be set as close to the experimental data as possible. The goal is then to obtain similar result from both experimental and simulation studies. Afterwards, the simulation setup can be used in optimization studies of the reservoir. As a result, we have a more fundamental understanding of our reservoir and its fluid flow. But this should be done after we have resolved the problem within the LBM implementation itself. This is done as a part of the data assimilation in reservoir management workflow.

Bibliography

Bhatnagar, P. L., Gross, E. P., Krook, M., May 1954. A model for collision processes in gases. i. small amplitude processes in charged and neutral one-component systems. Phys. Rev. 94, 511–525.
URL https://link.aps.org/doi/10.1103/PhysRev.94.511

Blunt, M. J., 2017. Multiphase Flow in Permeable Media: A Pore-Scale Perspective. Cambridge University Press.

D'Humières, D., Ginzburg, I., Krafczyk, M., Lallemand, P., Luo, L.-S., 04 2002. Multiple-relaxation-time lattice boltzmann models in three dimensions. Philosophical transactions. Series A, Mathematical, physical, and engineering sciences 360, 437–51.

Grucelski, A., Pozorski, J., 2013. Lattice boltzmann simulations of flow past a circular cylinder and in simple porous media. Computers & Fluids 71, 406 – 416.
URL http://www.sciencedirect.com/science/article/pii/S0045793012004380

Grunau, D., Chen, S., Eggert, K., 1993. A lattice boltzmann model for multiphase fluid flows. Physics of Fluids A: Fluid Dynamics 5 (10), 2557–2562.
URL https://doi.org/10.1063/1.858769

He, X., Luo, L.-S., 1997. Theory of the lattice Boltzmann method: From the Boltzmann equation to the lattice Boltzmann equation. Physical Review 56, 6811–6817.

Higuera, F. J., Succi, S., mar 1989. Simulating the flow around a circular cylinder with a lattice boltzmann equation. Europhysics Letters (EPL) 8 (6), 517–521.
URL https://doi.org/10.1209%2F0295-5075%2F8%2F6%2F005

Hou, S., Zou, Q., Chen, S., Doolen, G., Cogley, A. C., 1995. Simulation of cavity flow by the lattice boltzmann method. Journal of Computational Physics 118 (2), 329 – 347.
URL http://www.sciencedirect.com/science/article/pii/S0021999185711035

K. Gunstensen, A., H. Rothman, D., Zaleski, S., Zanetti, G., 05 1991. Lattice boltzmann model of immiscible fluids. Physical review. A 43, 4320–4327.

Latva-Kokko, M., Rothman, D. H., 2005. Diffusion properties of gradient-based lattice boltzmann models of immiscible fluids. Physical review. E, Statistical, nonlinear, and soft matter physics 71 5 Pt 2, 056702.

Leclaire, S., Parmigiani, A., Malaspinas, O. P., Chopard, B., Latt, J., 2017. Generalized three-dimensional lattice boltzmann color-gradient method for immiscible two-phase pore-scale imbibition and drainage in porous media. Physical Review.E 95 (3), 033306, iD: unige:97528.
URL https://archive-ouverte.unige.ch/unige:97528

Lenormand, R., 01 1999. Liquids in porous-media. Journal of Physics: Condensed Matter 2, SA79.

Lenormand, R., Zarcone, C., Sarr, A., 10 1983. Mechanisms of the displacement of one fluid by another in a network of capillary ducts. Journal of Fluid Mechanics 135.

Luo, L.-S., Liao, W., Chen, X., Peng, Y., Zhang, W., May 2011. Numerics of the lattice boltzmann method: Effects of collision models on the lattice boltzmann simulations. Phys. Rev. E 83, 056710.
URL https://link.aps.org/doi/10.1103/PhysRevE.83.056710

McClure, J. E., Li, Z., Sheppard, A. P., Miller, C. T., Jun 2018. An Adaptive Volumetric Flux Boundary Condition for Lattice Boltzmann Methods. arXiv e-prints, arXiv:1806.10589.

Pradipto, Purqon, A., jul 2017. Accuracy and numerical stabilty analysis of lattice boltzmann method with multiple relaxation time for incompressible flows. Journal of Physics: Conference Series 877, 012035.
URL https://doi.org/10.1088%2F1742-6596%2F877%2F1%2F012035

Qian, Y. H., D'Humieres, D., Lallemand, P., 1992. Lattice BGK Models for Navier-Stokes Equation. Vol. 17. pp. 479–484.

Ramstad, T., Berg, C. F., Thompson, K., May 2019. Pore-scale simulations of single- and two-phase flow in porous media: Approaches and applications. Transport in Porous Media.
URL https://doi.org/10.1007/s11242-019-01289-9

Shan, X., Chen, H., Mar 1993. Lattice boltzmann model for simulating flows with multiple phases and components. Phys. Rev. E 47, 1815–1819.
URL https://link.aps.org/doi/10.1103/PhysRevE.47.1815

Succi, S., 2001. The Lattice Boltzmann Equation: for Fluid Dynamics and Beyond. Oxford University Press.

Sukop, M. C., Thorne Jr., D. T., 2006. Lattice Boltzmann Modeling: An Introduction for Geoscientists and Engineers. Springer.

Zou, Q., He, X., 1997. On pressure and velocity flow boundary conditions and bounceback for the lattice Boltzmann BGK model. Phys Fluids 9, 1591–1598.

Appendix A

Boltzmann Equation

In this part, the Boltzmann Equation is derived. Firstly, we define the phase-space, μ, that contains the position and velocity of the particles. Further, we define a function $f(\vec{x}, \vec{v}, t)$ as a probability of finding a particle with position $\vec{x}$, velocity $\vec{v}$, and at time t. Integration over the whole phase-space will result in the number of particles:

$$\int f(\vec{x}, \vec{v}, t) d\mu = N \tag{A.1}$$

Here, we assume that all the particles are identical, i.e. they have the same size and mass. Moreover, we derive the equation for extremely dilute gas: the interparticle distance is much larger than the de Broglie wavelength of the gas particle,

$$\frac{nh^3}{(mk_BT)^{3/2}} \ll 1 \tag{A.2}$$

Where n is the particle density, h is the Planck's constant, m is the particle mass, k_B is the Boltzmann constant, and T is temperature. The above equation implies that Boltzmann Equation applies to a low density, high temperature gas. Now, we are observing a part of the phase space, μ_i. We observe the evolution of the particle in the phase space from the domain μ_i to μ_i'. Suppose an external force $\vec{F}$ exists and there is no collision involved. Since the number of particles have to be conserved, the following equation holds:

$$f(\vec{x}, \vec{v}, t) d\mu = f(\vec{x} + \vec{v}\Delta t, \vec{v} + \frac{\vec{F}}{m}\Delta t, t + \Delta t) d\mu \tag{A.3}$$

Since $d\mu = d\mu'$, the terms cancel out. Further, performing Taylor expansion will yields:

$$\left(\frac{\partial}{\partial t} + \vec{v} \cdot \nabla_{\vec{x}} + \frac{\vec{F}}{m} \cdot \nabla_{\vec{v}}\right) f = 0 \tag{A.4}$$

However, due to collision process, we can have loss of particles from the domain of interest to other part of the phase space. The number of particle lost per unit time is denoted as L. On the other hand, we can have gain of particles from the other part of the phase space to the domain of interest. The number of particle gain per unit time is denoted as G. Therefore, the equation can be expressed as:

$$\left(\frac{\partial}{\partial t} + \vec{v} \cdot \nabla_{\vec{x}} + \frac{\vec{F}}{m} \cdot \nabla_{\vec{v}}\right) f = G - L \tag{A.5}$$

or, if the original terms are used, then the expression is:

$$f(\vec{x} + \Delta x, \vec{v} + \frac{\vec{F}}{m}\Delta t, t + \Delta t) - f(\vec{x}, \vec{v}, t) = \left(\frac{\partial f}{\partial t}\right)_{col} dt \tag{A.6}$$

The collision term can be describing the collision process with the following assumptions:

- Binary collision: only two particles interaction can occur. Prior to the collision, the particles have a velocity of $\vec{v}_1$ and $\vec{v}_2$. After the collision, the particles have a velocity of $\vec{v}_1'$ and $\vec{v}_2'$.
- Elastic collision, meaning that the momentum is conserved ($\vec{v}_1 + \vec{v}_2 = \vec{v}_1' + \vec{v}_2'$) and the energy is conserved ($\vec{v}_1^2 + \vec{v}_2^2 = \vec{v}'^2_1 + \vec{v}'^2_2$).
- Molecular chaos: the particle distribution f_1 and f_2 are independent. Thus, if $f_{1,2}$ is the probability of finding both particles of velocity $\vec{v}_1$ and $\vec{v}_2$, then $f_{1,2} = f_1 f_2$

From scattering theory, we can compute the number of the particle that goes out of the domain due to this collision process:

$$L = \int d^3 v_2 \int d\sigma(g, \Omega) f_1 f_2 g$$

Here we define v_2 as the incident velocity, g as the magnitude of the relative speed of the particles, $d\Omega$ as the solid angle that the particle scattered towards, and $d\sigma(g, \Omega)$ as the differential cross section. For the gain term, we have the assumption that the collision we have previously is time invariant and that the probability of the collision and reverse

collision (i.e. prior velocities are $\vec{v}_1'$ and $\vec{v}_2'$ and the velocities after the collision are $\vec{v}_1$ and $\vec{v}_2$) are the same. Therefore, the gain term will have the form of:

$$G = \int d^3v_2 \int d\sigma(g,\Omega) f_1' f_2' g$$

This leads to the general form of Boltzmann Equation:

$$\left(\frac{\partial}{\partial t} + \vec{v}\cdot\nabla_r + \frac{\vec{F}}{m}\cdot\nabla_{\vec{v}}\right) f = \int d^3v_2 \int d\sigma(g,\Omega)(f_1' f_2' - f_1 f_2) g \tag{A.7}$$

Appendix B

Equilibrium distribution

From Equation A.7, we want to observe the equation at equilibrium. Suppose there is no external force. At equilibrium, there is no change in the distribution function, and the distribution is independent of space. As a consequence, all the terms in the l.h.s will cancel out. For the collision integral to also be zero, the term ${f'}_1^{eq} {f'}_2^{eq} - f_1^{eq} f_2^{eq}$ also has to be zero. This is proved by Boltzmann's H-theorem. Similar to the definition of entropy, we define the function $H(t)$ such that:

$$H(t) = \int d^3v f(\vec{v}, t) \ln f(\vec{v}, t) \tag{B.1}$$

Performing first derivation with respect to t to this function, we obtain:

$$\partial_t H(t) = \int d^3v \frac{\partial f(\vec{v}, t)}{\partial t} [1 + \ln f(\vec{v}, t)] \tag{B.2}$$

The analysis continues by evaluating this function by plugging in the collision term. We evaluate four conditions, with each available velocities. All the equations are then combined to get the following form:

$$0 = \int d^3v_1 \int d^3v_2 \int d\sigma(g, \Omega) g ({f'}_1^{eq} {f'}_2^{eq} - f_1^{eq} f_2^{eq}) \ln \left(\frac{{f'}_1^{eq} {f'}_2^{eq}}{f_1^{eq} f_2^{eq}} \right) \tag{B.3}$$

For the integral to be zero, we must have $f_1^{eq} f_2^{eq} = {f'}_1^{eq} {f'}_2^{eq}$. This condition is sometimes called as *detailed balance*. Now we perform logarithmic operation to both sides, we

obtain:

$$\ln f_1^{eq} + \ln f_2^{eq} = \ln f'^{eq}_1 + \ln f'^{eq}_2 \tag{B.4}$$

The above equation shows that the logarithmic operation is an additive collision invariant. Therefore, $\ln f$ must be a dependent on dynamic collision invariant: number, momentum, energy. Mathematically speaking,

$$\ln f^{eq}(\vec{v}) = A + B\vec{v} \cdot \vec{v}_0 + Cv^2 \tag{B.5}$$

where A, B, and C are the Lagrangian multipliers. The values are obtained by imposing the conserved parameters, as shown below:

$$m \int f d\vec{v} = \rho \tag{B.6}$$

$$m \int f v_a d\vec{v} = \rho \vec{u}_a \tag{B.7}$$

$$m \int f \frac{v^2}{2} d\vec{v} = \rho e \tag{B.8}$$

where $\vec{u}_a$ is the macroscopic flow speed and ρe is the energy density. Finally, we obtain Maxwell-Boltzmann equilibrium distribution function in D-spatial dimensions:

$$f^{eq}(\vec{q}) = \rho \left(\frac{m}{2\pi RT} \right)^{D/2} \exp\left\{ \left(-\frac{mq^2}{2RT} \right) \right\} \tag{B.9}$$

Here we use the so-called *peculiar speed*, $\vec{q} = \vec{c} - \vec{u}$, which is the relative speed of the particles with respect to the fluid (Succi, 2001). The equation is then approximated using Taylor expansion:

$$
\begin{aligned}
f^{eq} &= \rho\left(\frac{1}{2\pi RT}\right)^{D/2} \exp\left\{\left(-\frac{|\vec{c}-\vec{u}|^2}{2RT}\right)\right\} \\
&= \rho\left(\frac{1}{2\pi RT}\right)^{D/2} \exp\left\{\left(-\frac{\vec{c}^2}{2RT} + 2\frac{\vec{c}\cdot\vec{u}}{2RT} - \frac{\vec{u}^2}{2RT}\right)\right\} \\
&= \rho\left(\frac{1}{2\pi RT}\right)^{D/2} \exp\left\{\left(-\frac{\vec{c}^2}{2RT}\right)\right\} \exp\left\{\left(\frac{\vec{c}\cdot\vec{u}}{RT} - \frac{\vec{u}^2}{2RT}\right)\right\} \\
&= \rho\left(\frac{1}{2\pi RT}\right)^{D/2} \exp\left(-\frac{\vec{c}^2}{2RT}\right)\left[1 + \frac{\vec{c}\cdot\vec{u}}{RT} + \frac{(\vec{c}\cdot\vec{u})^2}{2(RT)^2} - \frac{\vec{u}^2}{2RT} + \dots\right]
\end{aligned}
$$

Equation 3.6 is obtained by truncating the expansion terms, setting $c_s = \sqrt{3RT}$, and setting the weight factor with the remaining terms. The consequence of this approximation is that the Mach number has to be sufficiently small, $Ma = |\vec{u}|/c < 0.1$ (Ramstad et al., 2019).

Appendix C

Discretization of phase-space

This appendix follows the paper by He and Luo (1997). The discretization of phase-space is done by solving the quadrature of the integral of equilibrium distribution function (Equation B.9) over velocity:

$$I = \int \psi(\vec{c}) f_i^{eq} d^3\vec{c} \approx \sum_i w_i \psi(\vec{c}) f_i^{eq} \tag{C.1}$$

where the function ψ is the hydrodynamic moments, and is in the form of polynomial of the microscopic velocity, $\vec{c}$. The hydrodynamic moments evaluated are:

$$\rho : 1, c_i, c_j \tag{C.2a}$$
$$\vec{u} : c_i, c_i c_j, c_i c_j c_k \tag{C.2b}$$
$$T : c_i c_j, c_i c_j c_k, c_i c_j c_k c_l \tag{C.2c}$$

First, we observe the $D2Q9$ case. Here, we define $\psi_{m,n}(\vec{c}) = c_x^m c_y^n$, then observe the l.h.s. of Equation C.1:

$$I = \frac{\rho}{\pi}(\sqrt{2RT})^{m+n} \left\{ \left(1 - \frac{\vec{u}}{2RT}\right) I_m I_n + \frac{2(u_x I_{m+1} I_n + u_y I_m I_{n+1})}{\sqrt{2RT}} + \right. \tag{C.3}$$
$$\left. \frac{u_x^2 I_{m+2} I_n + 2u_x u_y I_{m+1} I_{n+1} + u_y^2 I_m I_{n+2}}{RT} \right\} \tag{C.4}$$

Here we have used the equilibrium distribution function from Equation 3.6. To compute I_m, we choose the third-order Hermite formula, since we are using 9-bit model (3 bit for x- and y-direction). Here, $I_m = \int_{-\infty}^{\infty} e^{-\zeta^2} \zeta^m d\vec{c} = \sum_{j=1}^{3} \omega_j \zeta_j^3$, such that $\vec{\zeta} = \vec{c}/\sqrt{2RT}$. The three abcissas of the quadrature and their corresponding weight are:

$$\begin{aligned} \zeta_1 &= -\sqrt{3/2} & w_1 &= \sqrt{\pi}/6 \\ \zeta_2 &= 0 & w_2 &= 2\sqrt{\pi}/3 \\ \zeta_3 &= \sqrt{3/2} & w_3 &= \sqrt{\pi}/6 \end{aligned}$$

Plugging in I_m into Equation C.3 yields:

$$I = \frac{\rho}{\pi} \sum_{i,j=1}^{3} w_i w_j \psi(c_{i,j}) \left\{ 1 + \frac{(c_{i,j} \cdot \vec{u})}{RT} + \frac{(c_{i,j} \cdot \vec{u})^2}{2(RT)^2} - \frac{\vec{u}^2}{2RT} \right\} \tag{C.5}$$

Finally, from Equation C.5, we can identify the equilibrium distribution function:

$$f_{i,j}^{eq} = \frac{w_i w_j}{\pi} \rho \left\{ 1 + \frac{(c_{i,j} \cdot \vec{u})}{RT} + \frac{(c_{i,j} \cdot \vec{u})^2}{2(RT)^2} - \frac{\vec{u}^2}{2RT} \right\} \tag{C.6}$$

This results in the weight factor ω to be computed as

$$\omega = \frac{w_i w_j}{\pi} \tag{C.7}$$

For $D3Q27$ model, similar approach is done. Since we are dealing with 3-dimensional space, the moments evaluated are for three directions. Therefore, instead of having Equation C.5, now we will have

$$f_{i,j,k}^{eq} = \frac{w_i w_j w_k}{\pi^{3/2}} \rho \left\{ 1 + \frac{(c_{i,j,k} \cdot \vec{u})}{RT} + \frac{(c_{i,j,k} \cdot \vec{u})^2}{2(RT)^2} - \frac{\vec{u}^2}{2RT} \right\} \tag{C.8}$$

the weighting factor ω is then computed as

$$\omega = \frac{w_i w_j w_k}{\pi^{3/2}} \tag{C.9}$$